A time-dependent two-dimensional model simulation of lower ionospheric variations under intense SAID

Jun Liang[1], J.P. St-Maurice[2], and E. Donovan[1]

1. Department of Physics & Astronomy, University of Calgary, Canada

2. Institute of Space and Atmospheric Studies, University of Saskatchewan, Canada

Corresponding author: Jun Liang (liangj@ucalgary.ca)

Key points:

1.We present a 2D time-dependent model simulation of the self-consistent ionospheric variations of the Te, Ti, Ne, and FAC, under strong SAID

2. The ion Pedersen drift effect leads to strong depletion of density and conductance in the lower ionosphere in a large portion of SAID

3. We corroborate the presence of strong gradients of plasma density, temperature, and flows, in the lower ionosphere at the edge of SAID

Abstract. The subauroral ion drift (SAID) denotes a latitudinally narrow channel of fast westward ion drift in the subauroral region, often observed during geomagnetically disturbed intervals. The recently recognized subauroral optical phenomena, the Strong Thermal Emission Velocity Enhancement (STEVE) and the Picket Fence, are both related to intense SAIDs. In this study, we present a 2D time-dependent model simulation of the self-consistent variations of the electron/ion temperature, density, and FAC, under strong SAID, with more focus in the lower ionosphere. The anomalous electron heating in the E-region is evaluated using an empirical model. Our simulation reproduces many key features of SAID, such as the strong electron temperature enhancement in the upper F-region, the intense ion frictional heating, and the plasma density depletion. Most importantly, the ion Pedersen drifts is found to play a crucial role in the density variations and FAC dynamics in the lower ionosphere. The transport effect of ion Pedersen drifts leads to strong density depletion in the lower ionosphere in a large portion of SAID. The FAC inside SAID is mainly downward with magnitude $\leq \sim 1$ $\mu A/m^2$. At the poleward edge of SAID, the ion Pedersen drift leads to a pileup of the plasma density and an upward FAC. Our simulation results also corroborate the presence of strong gradients of plasma density, temperature, and flows, at the edge of SAID, which may be conducive to certain plasma instabilities. Our model provides a useful tool for the future exploration of the generation mechanisms of STEVE and Picket Fence.

Plain Language Summary

The recently recognized subauroral optical phenomena, the Strong Thermal Emission Velocity Enhancement (STEVE) and the Picket Fence, are inherently related to a special activity termed "subauroral ion drift (SAID)", namely a rapid (several km/s) westward drift of plasma in the Earth's ionosphere. Existing observations and models related to SAID are limited to the upper/topside ionosphere that is not where STEVE and Picket Fence emissions actually come from. In this study,

we present a model simulation of the variations of the ionospheric state under strong SAID. In particular, we mainly focus on the lower-altitude (<200 km) region where ions and electrons tend to move differently. The difference between the ion and electron motions leads to a redistribution of plasma densities and produce electric currents in the lower ionosphere across the SAID channel: density depletion and downward currents exist in the equatorward and center portion of SAID, while density pileup and upward currents exist near the poleward edge of SAID. A strong latitudinal gradient of plasma temperature, density, and flows, is formed at the edge of SAID. The ionospheric variations and structures across the SAID channel achieved from this study would help the exploration of the underlying mechanisms of STEVE and Picket Fence.

1. Introduction

During geomagnetically disturbed intervals, a latitudinally narrow yet longitudinally elongated zone of fast westward ion drift (or equivalently strong poleward electric field) often appears in the evening to midnight sector equatorward of the auroral oval. Galperin et al. [1973] first reported such phenomena and called them polarization jets. They were subsequently termed as "subauroral ion drift" (SAID) by Spiro et al. [1979]. References to early observations and to subsequent clarifications of the properties and signatures of SAID can be found in Anderson et al. [1993]. Later, Foster and Burke [2002] suggested an inclusive name, subauroral polarization streams (SAPS), to encompass both the narrow and intense SAIDs and the broader regions of relatively weaker westward subauroral plasma drifts [e.g., Yeh et al., 1991]. However, it is now generally recognized that SAID and SAPS (without SAID) differ in a number of fundamental aspects [Mishin et al., 2017; Nishimura et al., 2020]. SAIDs have been studied in both ground and space-based observations, such as in electric field measurements [e.g., Puhl-Quinn et al., 2007], radar

72 measurements [e.g., Foster et al., 1994], and ion drift measurements [Anderson et al., 1993, 2001;

73 Archer et al., 2018; 2019a; Nishimura et al., 2019; 2020]. Elevated electron/ion temperatures and

74 depleted electron densities are typically observed within SAID [Moffett et al. 1998; Andersen et

75 al., 1993; 2001; Archer et al.,2018; 2019a; Nishimura et al., 2020]. Motivated by the observations,

76 numerous model simulations of the ionosphere have been performed to study the ionospheric

77 processes related to the observed signatures of SAID, for example, the plasma density depletion

78 and electron temperature enhancement in the upper F-region [e.g., Moffett et al., 1992; 1998], and

79 the strong ion upflows in the topside ionosphere [e.g., Heelis et al., 1993].

80   In recent years, the recognition and observations of the Strong Thermal Emission Velocity

81 Enhancement (STEVE) and the Picket Fence optical phenomena have further lifted the research

82 interest in SAID. The generation mechanisms for the STEVE and Picket Fence remain unclear to

83 date. This stated, it is now well established that STEVE's are collocated with intense SAID

84 channels [Archer et al., 2019a; Nishimura et al., 2019; 2020; Chu et al., 2019], while Picket Fences

85 are situated in close vicinity, likely near the poleward edge, of STEVE [Gillies et al., 2020; Semeter

86 et al., 2020]. The consensus has now emerged that intense SAIDs have to play a pivotal role in the

87 generation of STEVE and Picket Fence optical emissions [Harding et al., 2020; Nishimura et al.,

88 2020; Semeter et al., 2020; Liang et al. 2021]. Important unresolved issues are: (1) a major

89 component of STEVE emissions is not from known atomic or molecular auroral optical emissions

90 but is instead made of a notably very wide broadband emission [e.g., Gillies et al, 2019; Liang et

91 al., 2019]; (2) the green line in the Picket Fence emissions is not accompanied by N_2^+ emissions

92 implying that the emissions may not be generated by an auroral type of electron precipitation [e.g.

93 Mende et al., 2019]. Existing studies on their emission altitudes have unveiled that, the Picket

94 Fence and the lower-altitude part of the STEVE occur in the lower ionosphere (<200 km) [Archer

4

95   et al., 2019b; Liang et al., 2019; Semeter et al., 2020] and possibly own their production

96   mechanisms to chemical/physical processes in the lower ionosphere [Liang et al., 2019; Hedin et

97   al. 2020; Semeter et al., 2020]. However, despite decades of observations and model simulations

98   of SAID, existing SAID-related studies have been mostly focused on the upper F-region/topside

99   ionosphere, yet the variations/structures in the E-region and lower F-region led by SAID is largely

100 unreported. The lack of definite knowledge about the lower ionospheric variations under intense

101 SAID hampers the exploration of the underlying mechanism of STEVE and Picket Fence.

102 The present study is motivated by the need to establish the state of the ionosphere in STEVE

103 and Picket Fences situations. A model specially tailored to SAID conditions is built for such a

104 research purpose. We shall investigate the plasma densities, temperatures, conductivities, and

105 electrodynamics in the lower ionosphere under the effect of an intense SAID channel. The plasma

106 densities in the region of interest need to be assessed in the presence of attendant Pedersen currents

107 known to carry plasma across the SAID channels [Banks and Yasuhara, 1978], and in the presence

108 of elevated electron/ion temperatures, including electron temperature enhancements from plasma

109 wave heating in the E region (e.g., St-Maurice and Goodwin [2021], and references therein). The

110 ionospheric variations and structures across the SAID channel achieved from this study would aid

111 in the ongoing exploration of the underlying mechanisms of STEVEs and Picket Fences.

112 Existing ionospheric models can be broadly categorized into three classes. The first class is a

113 1D model, e.g., the FLIP model [Richards, 2001], the GLOW model [Solomon et al., 1988], and

114 the now-termed TREx-ATM model [Liang et al., 2016; 2017]. They typically solve the plasma

115 parameters and/or the auroral emission rates along a magnetic field line. The second class is a

116 global 3D model, such as TIEGCM [Richmond et al., 1992], SAMI [Huba et al., 2000], and GITM

117 [Ridley et al., 2002], which typically simulates the evolution and structures of the global or

regional ionosphere (and thermosphere) under externally driving forces. However, the time/latitude resolution of those global models is not optimal for our specific research objective, namely the lower ionospheric variations in a narrow SAID channel. The third class of models is often 2D, and typically deals with certain specific small- or meso-scale structures, e.g., a precipitation-enhanced region with sharp boundaries [Noel et al., 2000; 2005; deBoer et al., 2010], the auroral downward current region [Zettergren and Semeter, 2012], and the ionospheric Alfven resonator [Sydorenko et al., 2013]. A noteworthy effort was done by deBoer et al. [2010], who also incorporated the ion Pedersen drift in their model and highlighted the role of ion Pedersen transport under a tilted field geometry in the lower ionospheric dynamics, though their research interest is focused on the discrete auroral arc with uniform ambient electric field yet sharp precipitation boundary. The model we develop and present in this paper belongs to the third class, and is specifically tailored to intense SAID conditions, with weak precipitation yet strong and narrow electric field structures. Most of the key physical processes that are understood or expected to play a role in SAID, such as the ion Pedersen transport, the anomalous electron heating, the ion upflows, and the enhanced vibrational excitation of N_2, are all incorporated into one synthesized model. The current paper is intended to serve as the first of a series of upcoming studies, based upon the developed model, to investigate more subtleties and anomalies of the ionospheric electrodynamics that could potentially contribute to the STEVE and Picket Fence production under a variety of SAID and ambient ionospheric conditions.

The rest of this paper is organized as follows. In section 2 we describe the basic equations and numerical schemes of our model. In section 3, we depict the ambient ionospheric condition surrounding STEVE that we shall use to set up our model runs. The simulation results are presented

in Section 4. We discuss a few important implications of our results in the context of the Picket

Fence phenomenon in Section 5 before reaching our conclusions in Section 6.

2. Model description

The model to be described and used in this study inherited from the Transition Region

Explorer Auroral Transport Model (TREx-ATM), which we had developed for years [Liang et al.,

2016; 2017]. For the specific research purpose of this study, we have made a few key

improvements to our previous model: (a) We extend the model to 2D (MLAT/altitude) geometry.

(b) We include the electron anomalous heating and the ion Pedersen drift, two pronounced effects

of intense SAID in the lower ionosphere, and the FAC is self-consistently computed from the

divergence of ion Pedersen currents. (c) In terms of chemical processes, while keeping all ion

species and excited neutrals in our previous model, we also consider the change of atomic nitrogen,

the nitric oxide, and the vibrational excitation of molecular nitrogen in the model. We emphasize

again that the main research interest of this study is in the lower ionosphere (<200 km altitude),

which enables us to make a few key assumptions/simplifications of our model. We first introduce

the geometry and those key assumptions/simplifications of our model as follows.

1. The SAID plasma convects in the azimuthal (y) direction that is deemed aligned with

magnetic L-shell. We assume an azimuthal homogeneity (i.e., $\partial/\partial y = 0$) throughout this study.

Anderson et al. [2001] suggested that SAID may exist simultaneously over at least ~3 h MLT.

Optical observations of STEVE also indicated that it might span over ~2.5 h MLT sectors

[Gallardo‐Lacourt et al., 2018b; Nishimura et al., 2020]. Therefore, the timescale of plasma

flowing through the SAID is longer than the other timescales of interest, e.g., that of the ion and

electron heating, and the density and FAC variation timescale related to the ion Pedersen drift, in

163 the lower ionosphere. That said, the finite azimuthal width of SAID has some effects in the upper

164 ionosphere where the variations tend to be more gradual, and may affect the interpretation of some

165 of our results in the upper F-region, as we shall elucidate later in Section 4.

166   2. While the electron/ion temperature and density are self-consistently calculated, the major

167 constituents of neutrals (such as N_2/O_2/O), as well as the neutral temperature, are kept unchanged

168 in our model. There is little doubt that ionosphere-thermosphere (IT) interaction is operative under

169 SAID, and there is evidence of such IT interaction based upon neutral observations in conjunction

170 with STEVE [Liang et al., 2021]. However, the coupling to the thermosphere and the resultant

171 change of major neutral constituents would presumably be less important in the lower ionosphere

172 at subauroral latitudes, where the plasma concentration is usually far lower than neutrals. We do

173 include the density variations of some minor neutral species, such as N, NO, and the vibrationally

174 excited N_2 in the model. We assume all neutrals to be stagnant, i.e., we neglect neutral winds.

175 2.1 Basic equations

176   In a nutshell, our model consists of the electron and ion energy equations, the continuity

177 equations of ions/electrons as well as some minor and excited neutrals, and the current continuity

178 equation. When the effect of viscous heating is ignored, the electron energy equation is given by

179 [e.g., Rees and Roble, 1975; Schunk and Nagy, 2009],

180
$$\frac{3}{2}k\frac{D}{Dt}(N_eT_e) = -\frac{5}{2}N_ekT_e\nabla\cdot\mathbf{u}_e - \nabla\cdot\mathbf{q}_e + Q_e - L_e \qquad , \qquad (1)$$

181 where

182
$$\frac{D}{Dt} = \frac{\partial}{\partial t} + \mathbf{u}_e\cdot\nabla \qquad ,$$

183 in which $\mathbf{u}_e$ is the electron bulk drift velocity, k is the Boltzmann constant, $\mathbf{q}_e$ is the electron heat

184 flow vector. Q_e is the electron heating rate which, in the context of SAID, consist of three parts:

190        $\mathbf{u_{e\perp}}$ and the other parallel to the magnetic field $u_{e//}$. For ionospheric

191 electrons the perpendicular component is essentially E×B convective drift which is virtually

192 incompressible in the ionosphere, so that $\nabla \cdot \mathbf{u}_{e\perp} \approx 0$. The electron Pedersen drift starts to matter

193 at below ~100 km, which is in practice close to the bottom boundary of our model. The explicit

194 expression of $u_{e//}$ is to be given in equation (10) later in this section. Using the continuity equation,

195
$$\frac{\partial N_e}{\partial t} + \nabla \cdot (N_e \boldsymbol{u}_e) = P_{ne} - L_{ne} \qquad , \qquad (2)$$

196 in which P_{ne} and L_{ne} denote the production and loss of electrons due to precipitations and chemical

197 reactions, equation (1) can be converted to,

198
$$\frac{3}{2} N_e k \frac{\partial T_e}{\partial t} = -\frac{3}{2} k T_e (P_{ne} - L_{ne}) - \frac{3}{2} N_e k u_{e//} \cdot \nabla_{//} T_e - N_e k T_e \nabla_{//} u_{e//} - \nabla_{//} q_{e//} + Q_e - L_e . \quad (3)$$

199 Note that in our geometry the electron E×B drift is along the y-direction, and $\partial/\partial y = 0$ is assumed

200 in our 2D model, so that the perpendicular advective term vanishes for electrons. Also, we have

201 neglected the perpendicular heat flow component which is usually much smaller than the parallel

202 heat flow for ionospheric electrons [Schunk and Nagy, 2009].

203   The ion energy equation can be derived similarly,

204
$$\frac{3}{2} N_i k \frac{\partial T_i}{\partial t} = -\frac{3}{2} k T_i (P_{ni} - L_{ni}) - \frac{3}{2} N_i k \boldsymbol{u}_i \cdot \nabla T_i - N_i k T_i \nabla \cdot \boldsymbol{u}_i + Q_{Ji} - L_{ie} - L_{in} \qquad , \qquad (4)$$

205   in which Q_{Ji} represents the ion heating rate due to the friction Joule heating. L_{ie} and L_{in} represents

206   the cooling rate due to collisions with electrons and neutrals, respectively. Note that in deriving (4)

207   we have also implicitly utilized the ion continuity equation,

208
$$\frac{\partial N_i}{\partial t} + \nabla \cdot (N_i \boldsymbol{u}_i) = P_{ni} - L_{ni} \ .$$
(5)

209   The ion drift velocity $\mathbf{u_i}$ in equation (4) and (5) is given by

210
$$\mathbf{u}_i = \frac{\kappa_i^2}{1+\kappa_i^2}\frac{\mathbf{E}\times\mathbf{B}}{B^2} + \frac{\kappa_i}{1+\kappa_i^2}\frac{\mathbf{E}}{B} + \mathbf{u}_{i//} \qquad ,$$
(6)

211   in which κ_i is the ratio between the ion gyrofrequency and the ion-neutral collision frequency. The

212   ion parallel drift $u_{i_{//}}$ is to be given in equation (9) later. Note that equation (6) represents a steady-

213   state solution of the ion momentum equation. The underlying rationale of such a treatment is that,

214   at the ionospheric altitudes of interest the steady-state ion drift is established at an ion-neutral

215   collisional timescale, much faster than other transport or chemical timescales of interest in our

216   model. Furthermore, the pressure-gradient drifts and diamagnetic drifts are ignored. We infer from

217   our simulation result that, even in the presence of strong heating within SAID, the pressure-

218   gradient associated perpendicular drift is still found to be 3 orders of magnitude smaller than the

219   electric drift, so that the former is ignored. The first two terms on the right-side of equation (6) are

220   conventionally called "Hall drift" and "Pedersen drift", respectively. As in the case for electrons,

221   the Hall drift does not play a role in the equation under the azimuthally homogeneous geometry.

222   The ion Pedersen drift however, can be very important to the plasma dynamics in the lower

223   ionosphere. As can be inferred from equation (6), the maximum ion Pedersen drift can be up to

224   half the SAID flow velocity. For our research interest of the STEVE-related SAID, whose width

225   is typically no more than a few tens of km, ions traverse the SAID channel in tens of seconds under

226   the enhanced Pedersen drift. This can be faster than the recombination rate of ions in the subauroral

227 ionosphere. Thus, the transport effect led by the SAID-enhanced ion Pedersen drift may act as the

228 principal process controlling the density variations in the lower ionosphere, as first suggested by

229 Banks and Yasuhara [1978]. The Pedersen drift is dependent upon ion species. In our model, we

230 consider the Pedersen drift of three major ions in the ionosphere, NO^+, O_2^+, and O^+.

231 It should be noted that we actually model the so-called "average" ion temperature in equation

232 (4). (a) The temperature is averaged over all ion species. In practical calculation, all heating and

233 cooling sources in equation (5) are summed over ion species, and $\mathbf{u_i}$ in equation (6) represents the

234 density-averaged bulk drift velocity of NO^+, O_2^+, and O^+. (b) The temperature is averaged over

235 the parallel and perpendicular directions. For more explanations of the implication of such an

236 average ion temperature under frictional heating and its partitioning into parallel and perpendicular

237 directions, see St-Maurice et al. [1999] and Goodwin et al. [2018]. Such an average ion

238 temperature suffices for most of our research purpose (e.g., calculating reaction rates). However,

239 we shall consider the temperature anisotropy and rectify the O^+ $T_{i//}$ when we calculate the

240 ambipolar diffusion velocity (see details later in this section).

241 We have neglected the ion heat flow conduction in the ion energy equation. The ion heat flow

242 is generally believed to be likely much smaller than the electron heat flow [e.g., Rees and Roble,

243 1975], though to the authors' knowledge a definite value of the ion heat flux has not yet been

244 reliably evaluated experimentally in the existing literature. It was also ignored in some existing

245 ionospheric models such as TIEGCM [Wang et al., 1999]. As we shall elucidate in the upcoming

246 simulation results, under intense SAID the frictional heating is extremely strong over a broad range

247 of altitudes, and the response time of the ion temperature to the frictional heating is very fast in

248 the lower ionosphere. In fact, T_i is basically determined by a local equilibrium between the

249 frictional heating and the collisional cooling with neutrals over the ionospheric altitudes of interest.

250 We have numerically tested and found that the inclusion of ion heat conduction (as in our previous

251 model Liang et al. [2017]) introduces trivial only changes to the T_i profile in the lower ionosphere,

252 but incurs heavy computational time costs. Therefore, based upon the above theoretical and

253 practical considerations we ignore the heat conduction in the ion energy equation for the specific

254 purpose of this study.

255 The parallel electron and ion drifts in equations (3) and (6) are derived from the steady-state

256 solution (and neglecting advective terms) of the ion and electron momentum equations.

257 $$-N_i m_i \nu_{in} u_{i//} - N_i m_i \nu_{ie} (u_{i//} - u_{e//}) - \nabla_{//} p_{i//} - N_i m_i g + N_i e E_{//} = 0 \qquad (7)$$

258 $$-N_e m_e \nu_{en} u_{e//} - N_e m_e \sum \nu_{ei} (u_{e//} - u_{i//}) - \nabla_{//} p_{e//} - N_e m_e g - N_e e E_{//} = 0 \qquad (8)$$

259 Neglecting terms of the order of m_e/m_i , together with $j_{//} = n_e e (\sum u_{i//} - u_{e//})$ these parallel

260 drifts are solved as,

261 $$u_{i//} = -\frac{g_{//}}{\nu_i} - \frac{\nabla p_{i//}}{N_i m_i \nu_i} - \frac{\nabla p_{e//}}{N_e m_i \nu_i} \qquad (9)$$

262 $$u_{e//} = -\frac{j_{//}}{N_e e} + \frac{\sum N_i u_{i//}}{N_e} \qquad (10)$$

263 in which $g_{//}$ denotes the field-aligned component of the gravitational acceleration. $p_{i//}$ and $p_{e//}$

264 denote the parallel ion and electron pressure, respectively. The sum in (8) and (10) is over ion

265 species. O^+ is often the dominant ion species in the upper/topside ionosphere where the ambipolar

266 diffusion becomes important, so that in some existing models (such as TIEGCM), only the

267 ambipolar diffusion of O^+ is considered. However, for our specific research interest, NO^+ is found

268 to replace O^+ to become the major constituent in the upper F-region under intense SAID. Therefore,

269 we shall consider two ion species, NO^+ and O^+, for the ambipolar diffusion in our model. For these

270 two ions, their parallel flux $n_i u_{i//}$ is rewritten in the following form,

$$271 \quad (N_i u_{i//})^{O+} = -g_{i//}(\frac{N_i}{v_{in}})^{O+} - k \cdot \frac{(\nabla T_{i//})^{O+} + \nabla T_{e//}}{(m_i v_{in})^{O+}}(N_i)^{O+} - k \cdot \frac{(T_{i//})^{O+} + T_{e//}}{(m_i v_{in})^{O+}} \cdot \nabla(N_i)^{O+}$$

$$272 \quad - \frac{kT_{e//}}{N_e(m_i v_{in})^{O+}} \cdot [(N_i)^{O+} \cdot \nabla(N_i)^{NO+} - (N_i)^{NO+} \cdot \nabla(N_i)^{O+}]$$

$$273 \quad (N_i u_{i//})^{NO+} = -g_{i//}(\frac{N_i}{v_{in}})^{NO+} - k \cdot \frac{(\nabla T_{i//})^{NO+} + \nabla T_{e//}}{(m_i v_{in})^{NO+}}(N_i)^{NO+} - k \cdot \frac{(T_{i//})^{NO+} + T_{e//}}{(m_i v_{in})^{NO+}} \cdot \nabla(N_i)^{NO+}$$

$$274 \quad - \frac{kT_{e//}}{N_e(m_i v_{in})^{NO+}} \cdot [(N_i)^{NO+} \cdot \nabla(N_i)^{O+} - (N_i)^{O+} \cdot \nabla(N_i)^{NO+}]$$

275 $\hspace{12cm}$ (11)

276 The superscript in (11) denotes the ion species. We have used the approximation $n_e \approx (n_i)^{NO+} +$

277 $(n_i)^{O+}$ in the derivation. The calculation of the ambipolar diffusion velocity involves the parallel

278 electron/ion pressure. The electron pressure is assumed to be isotropic in our model. It is however

279 known that ions, especially O^+, can become notably anisotropic in the presence of strong frictional

280 heating [St-Maurice et al., 1999; Goodwin et al., 2018]. More quantitively, Via Monte Carlo

281 simulations Goodwin et al. [2018] showed that, when the ion-ion and ion-electron collisions are

282 considered, the O^+ ion temperature is essentially isotropic for ion drift $u_{i\perp} < 800$ m/s, but the parallel

283 temperature is about half of the average temperature at $u_{i\perp} \sim 4$ km/s. In this regard, we use the

284 following empirical formula fitted from the ratio between $T_{i//}$ and the average T_i versus different

285 ion drift velocity for O^+ ions, in the study of Goodwin et al. [2018]:

$$286 \quad T_{i//}^{O+} = \begin{cases} T_n + (T_i^{ave} - T_n) \cdot [1 - 3.507 \times 10^{-4}(u_{i\perp} - 800) + 6.076 \times 10^{-8}(u_{i\perp} - 800)^2] & u_{i\perp} > 800 \ m/s \\ T_i^{ave} & u_{i\perp} < 800 \ m/s \end{cases}$$

287 in which T_i^{ave} represents the average ion temperature solved from equation (4), and T_n is the

288 neutral temperature. For the NO^+ ions, its parallel temperature is much closer to the average

289 temperature. More specifically, even at $u_{i\perp} \sim 4$ km/s, contingent on the background neutral

290 concentration the NO^+ parallel temperature is found to be $\sim 80\%$-86% of the average temperature

291 [Goodwin et al., 2018]. Therefore, NO^+ ion temperature is deemed isotropic in our model.

292   The FAC is computed according to the current continuity equation,

$$\nabla_{//} \cdot j_{//} + \nabla_{\perp} \cdot (\sum N_i e \mathbf{u_{i\perp}}) = 0 \tag{12}$$

294   The existence of FAC and the ambipolar diffusion naturally implies the presence of a parallel

295   electric field $E_{//}$, which can be derived from equation (8). Except for the Alfvenic process which

296   is not considered in our model, the electric field in the ionosphere is approximately electrostatic.

$$\mathbf{E}_{//} = -\nabla_{//}\Phi = \frac{j_{//}}{\sigma_{//}} - \frac{\nabla_{//}p_e}{N_e e} - \frac{m_e v_{en}}{N_e e} \sum N_i u_{i//} \quad , \tag{13}$$

$$\mathbf{E}_{\perp} = -\nabla_{\perp}\Phi \tag{14}$$

299   in which Φ is the electric potential, $\sigma_{//} = N_e e / m_e (v_{en} + \sum v_{ei})$ is the parallel conductivity. The

300   electron gravity is ignored here. The last term in (13) is often dismissed in the existing literature

301   [e.g., Schunk and Nagy, 2009] under the assumption that the ion ambipolar drift is much slower

302   than the electron drift as the FAC carrier. This condition may become marginal in intense SAID

303   cases with very strong ion upflows yet moderate FAC intensity [e.g., Heelis et al., 1993; Nishimura

304   et al., 2020]. Such a term is included in our model simulation. The perpendicular electric field

305   would change with the perturbed electric potential. This modifies the ion Pedersen drift and in turn

306   the FAC. Such an interaction/feedback between the electric field and the FAC was found to be

307   capable of generating fine structures of electric fields (including $E_{//}$) under some circumstances

308   [e.g., Noel et al., 2000; deBoer et al., 2010].

309   Our model also contains 7 excited/minor neutrals (see supplementary material). They all follow

310   the continuity equation in the same format as (2), but without the transport term since no neutral

311   wind is considered in our model. The calculation of the vibrationally excited populations of N_2

312   will be specifically addressed later in Section 2.3.

313   Equations (2) through (14) constitute the basic equation set of our model. Except for the

314   anomalous electron heating, which will be specifically discussed in the next subsection, all other

315   heating and cooling rates, as well as all chemical reactions involved in this study, are provided in

316   supplementary material. A special note is given here. Since our research objective features

317   extremely high electron and ion temperatures, and that many reactions are temperature dependent,

318   special care has been taken in checking the validity of empirical formulas of reaction rates at higher

319   electron/ion temperature. In particular, some of the published empirical rates are based upon

320   polynomial fitting of measured data in a certain range of temperature, and may not necessarily

321   guarantee their validity beyond the intended temperature range. Our general scheme is that, if there

322   are several reported empirical formulas with different validity ranges of temperature, we choose

323   to adopt the one that has the highest upper temperature bound and/or is convergent toward high

324   temperature. For example, for the dissociative recombination between O^+ and molecular neutrals,

325   the reaction rates used in this study are from St.-Maurice and Laneville [1998], which remain valid

326   for an effective ion temperature up to ~30000 K. Upon a careful check of all temperature-

327   dependent rates in our model, we notice that many of them are indeed fairly stable toward high

328   temperature, even beyond the labeled upper temperature limit. For a few rate formulas that seem

329   not to be convergent beyond the given upper temperature limit, when the simulated temperature is

330   exceedingly high, we shall use the rate value at the upper temperature limit.

331   2.2 Anomalous electron heating (AEH)

332   An accurate calculation of T_e led by AEH is a formidable or even unachievable task at the

333   current stage. First, a rigorous and computationally manageable theory of AEH is still lacking to

334   date. Secondly, existing observations of AEH under very strong convection flows (V_E > 3 km/s)

335   are somehow scarce. This is not only because larger V_E is geophysically rare, but also due to that

336 the signal strength may fall below the Incoherent Scatter Radar (ISR) detectability levels due to

337 large electron‐ion temperature ratio [Bahcivan, 2007]. Thus, instead of a rigorous theory and

338 solution of AEH, our model goal is to make the best attempts toward a reasonable estimate of T_e

339 in the E-region under intense SAID, based upon available AEH observations.

340 While it is known that the AEH stems from certain E-region instability/turbulence, the current

341 state of E-region instability theory does not give us accurate spectra of the density and electric

342 field perturbations as a function of the external electric field and ionospheric parameters. Some

343 simplified models of nonlinearly saturated disturbance, albeit all heuristic to a certain degree, were

344 usually applied to evaluate AEH in the E-region ionosphere [e.g., Robinson, 1986; Dimant and

345 Milikh, 2003]. One noteworthy attempt along this route was the Dimant and Mikilh [2003]

346 (hereafter referred to as DM03) model. Though based upon a few heuristic assumptions and

347 simplifications (see Hysell et al. [2013]), the DM03 model has achieved certain success and

348 practical applicability [deBoer et al., 2010; Dimant and Oppenheim 2011a; 2011b; Liu et al., 2016].

349 For the purpose of this study, we have extensively tested the DM03 model against the realistic

350 AEH events assembled in St-Maurice and Goodwin [2021]. We find that the DM03 results in

351 general show acceptable agreement with realistic observations for convection velocity V_E <2 km/s,

352 but tend to deviate notably from realistic observations for V_E >2 km/s. We footnote that, to the

353 authors' knowledge existing comparisons between AEH theories and observations were usually

354 limited to V_E <2 km/s [Milikh and Dimant 2003; Williams et al., 1992]. St-Maurice and Goodwin

355 [2021] suggested that the anomalous heating rate may be approximated by a 3rd-order polynomial

356 of V_E for V_E <~2 km/s, but is better described by a 4th-order polynomial when V_E is larger. This

357 finding partly explains why the agreement between the simulated T_e and the observations becomes

358 relatively poor at strong V_E (>2 km/s), since the DM03 (and also Robinson [1986]) heating rate

359   basically represents a 3rd-order polynomial of V_E. On the other hand, the DM03 model also

360   incorporates a kinetic modification of the electron cooling rate, which was inferred from a kinetic

361   simulation [Milikh and Dimant 2003] that is not easily replicated in our model.

362   We elect to resort to the approach of an observation-based empirical model. Recently, the

363   behavior of AEH was revisited by St-Maurice and Goodwin [2021] based upon a rich dataset of

364   realistic observations; a strong tendency of linear dependence of E-region electron temperature

365   versus electric field magnitude is found in their study. A similar conclusion was also reached in

366   Foster and Ericson [2000]. More specifically, St-Maurice and Goodwin [2021] suggest the

367   following empirical formula,

368    $$T_e = T_{e0} + S \cdot (V_E - 800\text{m/s}) \quad . \tag{15}$$

369   T_{e0} represents a base level when the AEH is supposed to play little or none effect ----- the instability

370   leading to AEH is supposed to have an E-field threshold, e.g., see equation 14 in DM03). V_E

371   represents the F-region ion flow observed by ISR (on average from ~300 km altitude), which

372   essentially yields the E×B convection drift. T_{e0} is expected to be event-dependent, contingent upon

373   parameters such as the ambient neutral temperature and other heating/cooling sources at play. In

374   our model, we resolve T_e with all other heating and cooling sources (in the absence of AEH but

375   including the classical frictional heating) for V_E up to 800 m/s, and hereby determine T_{e0}. V_E is

376   evaluated according to the E-field at 300 km altitude. The slope S used in our model is based upon

377   St-Maurice and Goodwin [2021]; the values in their Table 1 are slightly smoothened and

378   interpolated to our model grids in the 100-120 km altitude range. Figure 1 displays the altitudinal

379   profile of S used in our model. In supplementary material, we provide a simple subroutine that can

380   be used to evaluate the enhancement of T_e under AEH with the convection flow strength V_E,

381   without the necessity of complicated modeling effort. We also point out that, though a complete

382 theory of AEH is unavailable to date, according to existing theories and reasonable theoretical

383 expectations, the AEH heating rate and the dominant cooling terms (elastic and inelastic collisions

384 with neutrals) would presumably all be proportional to the electron density. Therefore, the AEH

385 T_e enhancement is expected to be insensitive to electron density variations [e.g., Liu et al., 2016].

386 One may question that, since existing AEH observations are generally limited to V_E <3.5 km/s,

387 we may have to assume a linear extrapolation beyond that range. St-Maurice and Goodwin [2021]

388 suggested that the linear trend may sustain to higher V_E, since the aspect angle of the plasma

389 instability structures responsible for the heating is basically proportional to the ambient electric

390 field. Readers are referred to their paper for more theoretical details of their proposal. To partially

391 relieve the uncertainty in extrapolation, in the following run we shall use a peak V_E of ~4 km/s --

392 - this is not up to the extreme SAID events in existing reports, but fairly close to (when mapped to

393 the Swarm altitudes) the median value of Swarm observations of STEVE-related SAID events as

394 reported in Archer et al. [2019a]. Given the current status of AEH theories and observations under

395 intense V_E , it is fair to say that neither a semi-heuristic model approach (such as DM03) nor an

396 empirically data-based approach can be completely free of uncertainty, and it is difficult to assert

397 which approach is inherently better. Anyway, the empirical approach we elect to use is

398 incontrovertibly advantageous in computation efficiency. We have made test runs using DM03 for

399 the AEH module and found that, while the DM03 model may produce somehow different T_e profile

400 in the E-region, the major results of this study, such as the plasma depletion and conductance

401 reduction in the lower ionosphere, are not qualitatively changed.

402 2.3 Vibrationally excited N_2 distribution

403 Under SAID, the vibrational excitation of N_2 plays an important role in the electron density

404 depletion in the upper/topside ionospheric altitude where T_e is significantly elevated. In short, N_2^*

405 at higher vibration levels has a much faster reaction rate with O^+ and thus effectively converts O^+

406 to NO^+. Since NO^+ has a faster recombination rate than O^+, the total plasma density is reduced

407 accordingly. However, as explained in Campbell et al. [2006], a time step simulation is not

408 practical for the calculation of N_2^* populations because the wide range of radiative transition

409 probabilities would require a prohibitively large number of small time intervals. As done in many

410 previous studies [e.g., Cartwright et al., 2000; Campbell et al., 2006], in our model we consider

411 only the steady-state equilibrium distribution of the vibrationally excited N_2 states. The equation

412 for the statistical equilibrium of each vibrational level υ of N_2 is given by,

414
$$k_{\upsilon 0} n_0 + \sum_K CP_v^K + \sum_i A_{i\upsilon} n_i + \sum_i VV_{(\upsilon\pm 1)\upsilon}^{(i\mp 1)i} n_{\upsilon\pm 1} n_{i\mp 1} + Q_{\upsilon+1} n_{\upsilon+1}$$

415
$$= \left(\sum_i A_{\upsilon i} + \sum_K CL_v^K + \sum_i VV_{\upsilon(\upsilon\pm 1)}^{i(i\mp 1)} n_i + Q_\upsilon \right) \cdot n_\upsilon$$

413 $\hspace{12cm}$ (16)

416 in which $k_{\upsilon 0}$ denotes the electron impact excitation rate of vibrational level υ (we assume the

417 impact excitation stems from the ground state with density n_0). CP_v^K and CL_v^K denote the

418 production and loss rate of vibrational level υ due to chemical reactions. $A_{i\upsilon}$ is the transition

419 probability between the vibrational level υ and i. $VV_{(\upsilon\pm 1)\upsilon}^{(i\mp 1)i}$ is the rate of vibrational exchange

420 where a collision between levels $\upsilon \pm 1$ and $i \mp 1$ leaves them in level υ and i. Q_υ is the rate of

421 stepwise quenching of level N_2^* by collisions with O atoms. The vibration-translational transition

422 and the molecular diffusion of N_2 are ignored in the model. We consider up to the 10th level of the

423 vibrational N_2 state. For other details of the calculation of N_2^* distribution, see Newton et al. [1974],

424 Cartwright et al. [2000], and Campbell et al. [2006]. The calculation of electron impact excitation,

425 as well as all N_2^*-involved chemical processes and their reaction rates, are identical to those in

426 Campbell et al. [2006]. The vibrational-vibrational exchange rate is from Newton et al. [1974].

427 The transition probabilities between vibrational levels are from Parlov [1998]. Note that the

428 vibrational excitation of N_2 is also one of the major electron cooling processes, and the cooling

429 rate is self-consistently calculated from the transition probability coefficients in our model.

430 Once the N_2^* distribution is determined, we use the formula in St.-Maurice and Laneville [1998]

431 for the reaction rate between O+ and ground-state N_2, and use the coefficients in Schmeltekopf et

432 al. [1968] for the relative enhancement of reaction rates at higher vibrational levels of N_2 (see table

433 S3 in supplementary material). An effective reaction rate between O^+ and N_2 is calculated

434 accordingly [e.g., Campbell et al., 2006].

435 2.4 Numerical Scheme

436 The energy equations and the continuity equations are solved alternatively using a Strang time-

437 splitting approach. Schematically, T_e and T_i advance at the integer time grid ($t^n \rightarrow t^{n+1}$), while

438 the ion densities of all species and FAC advance at the half-integer time grid ($t^{n-1/2} \rightarrow t^{n+1/2}$).

439 Note that as our convention here the upper script denotes the timestep. A dipole magnetic field

440 configuration is used in the model. The spatial grid is two-dimensional: one along a dipole filed

441 line and equally spaced in the vertical (z) direction, the other horizontally along the magnetic

442 meridian (x-direction, positive northward) and equally spaced in MLAT in an Altitude-adjusted

443 Corrected Geomagnetic (AACGM) sense [*Baker and Wing*, 1989]. In all simulation runs presented

444 in this paper, we adopt a time step of 0.1 s. The vertical grid interval is 1 km and the horizontal

445 grid resolution is 0.025^0 MLAT. In such a grid coordinate system, using Jacobi transform we

446 express the parallel and perpendicular gradient operator as $\nabla_{//} = \frac{\partial}{\partial s} = \frac{\partial}{\partial z} sinI$, $\nabla_\perp = \frac{\partial}{\partial x} cscI +$

447 $\frac{\partial}{\partial s} ctgI$, in which I is the magnetic dip angle.

448   One major challenge in the implementation of our model lies in the dramatic differences among,

449   and the altitudinal variations of, the timescales of the chemical/physical processes involved. To

450   deal with such a difficulty, we use a combination of the steady-state solution, the Runge-Kutta

451   method, and the numerical difference approach, in our numerical scheme. At altitudes below 120

452   km, the heating rates for both electrons and ions are strong, and the response timescales of T_e and

453   T_i , which are controlled by the electron- and ion-neutral interactions, are very fast (timescale

454   typically on order of ~0.1s or smaller). Therefore, at those altitudes we adopt a steady-state solution

455   for T_e and T_i, For V_E>800 m/s, T_e is obtained from equation (15). For T_e with V_E<800 m/s and T_i,

456   we neglect the time derivative and non-local terms in equations (3) and (4) and jointly solving the

457   two energy equations via Newton's method [Press et al., 2007]. This also sets up the bottom

458   boundary condition for subsequently solving the time-dependent electron/ion energy equations.

459   Note that we still consider the time evolution of the plasma density and FAC at altitudes <120 km,

460   since the chemical reaction timescales and the transport timescale led by the ion Pedersen drift and

461   are typically much longer than 0.1s.

462   Above 120 km, the time evolutions and non-local transport effect of T_e and T_i are considered.

463   The energy equations are solved using a semi-implicit finite difference method; the involved

464   difference schemes are similar to that in Huba et al. [2000] and Zhu et al. [2016]. Schematically,

465   the model uses the backward difference for the time derivative. Each source term partially

466   containing a linear dependence on the temperature is split into two parts, one with a linear

467   dependence, and the other without the linear dependence. The linear terms are evaluated at the

468   current timestep t^n, while the other terms are evaluated at the previous timestep t^{n-1}. The plasma

469   density involved in the energy equation is taken as the value at the previous half timestep $t^{n-1/2}$.

470   For example, the electron cooling term due to elastic collision with neutrals is expressed as $L_{en} =$

471     $Q_n\left(N_e^{n-1/2}, T_e^{n-1}\right) \cdot [T_e^n - T_n]$, in which $Q_n(N_e, T_e)$ is a nonlinear function of T_e dependent on

472   neural species [Schunk and Nagy, 2009]. The above semi-implicit method is found to be

473   numerically stable. An upwind difference scheme is used in treating the advective term in the

474   ion/electron energy equation. The electron/ion field-aligned drifts are calculated according to

475   equations (9) and (10). However, the terms involving the temperature gradients in (9) and (10) are

476   dropped in electron/ion energy equations. For the electron energy equation which involves thermal

477   conduction, the upper boundary of our model is set at 800 km altitude, where an external electron

478   heat flow is imposed as the upper boundary condition.

479   The electron and ion energy equations are weakly coupled via an electron-ion collision term.

480   In the lower ionosphere, the electron-ion collision is fairly minor compared to other

481   heating/cooling terms. In our algorithm, in each time step, T_e and T_i are first solved separately with

482   their own energy equation by using values in the previous time step in the electron-ion collision

483   term. We then adopt an iterative approach to obtain convergent solutions of T_e and T_i , i.e., we

484   replace T_i or T_e in the electron-ion collision term with the last obtained values and iterate. In

485   practice, we find that at most two iterations generally suffice for convergent solutions of T_e and T_i

486   with satisfying precision, namely that the relative difference of T_e and T_i between two successive

487   iterations is smaller than 10^{-5} at all altitudes of interest as our criterion.

488   The densities of ions and minor neutrals are solved at the half-integer time grid. A similar semi-

489   implicit method is also applied to the continuity equations of ion and neutral species involved

490   (except for the vibrationally excited N_2). We use the backward difference for the time derivative.

491   At each timestep $t^{n+1/2}$, the production rate is evaluated at the previous timestep $t^{n-1/2}$, while the

492   loss rate is written in the form $L_i = \mathcal{L}N_i = \mathcal{L}(t^{n-1/2}) \cdot N_i^{n+1/2}$. T_i^n and T_e^n obtained at the time

493   step t^n are used in calculating the temperature-dependent reaction coefficients. We take into

494 consideration of the Pedersen drift of NO^+ , O_2^+ , and O^+ in their continuity equations up to 350

495 km altitudes. We adopt the "donor cell" numerical scheme [Huba et al., 2000] in treating the

496 Pedersen transport term. For minor ions N^+ and N_2^+ , their chemical loss timescale tends to be

497 shorter than the Pedersen transport, so that we ignore the latter and use the 4th-order Runge-Kutta

498 method to solve their time-evolving continuity equations. While each ion or neutral species is

499 solved separately, we again apply an iterative approach (with similar procedure and criterion to

500 that described for T_e and T_i) to obtain convergent solutions of all densities involved. For the

501 vibrationally excited N_2, we only compute the steady-state solution by solving the equation set (17)

502 via Newton's method. The bottom boundary is set at 90 km. At this altitude, the ionosphere is

503 assumed to be under a steady-state local chemical balance; all transport terms related to the

504 Pederson drift and the ambipolar diffusion are dismissed. The upper boundary condition is to be

505 discussed later in this subsection. As to the boundary conditions in the latitudinal direction, the

506 lower-latitude boundary is set at where V_y is constant zero as per our SAID specification (see

507 equation 19 later), so that the plasma density at this lower boundary is solved in 1D geometry

508 without the Pedersen transport. The unidirectional (always poleward) property of the Pedersen

509 drift and our numerical scheme imply that no poleward boundary condition is required.

510 Our numerical scheme to treat the ambipolar diffusion term is briefly described as follows.

511 Following equation (11), the continuity equations for O^+ and NO^+ densities become two second-

512 order partial differential equations. We focus on the description of how we treat the term of the

513 form $\frac{\partial}{\partial z}\left[a(z,t)\frac{\partial N}{\partial z}\right]$. Without losing generality the continuity equation can be written in the form:

514
$$\frac{\partial N}{\partial t} = \frac{\partial}{\partial z}\left[a(z,t)\frac{\partial N}{\partial z}\right] + f(N,\frac{\partial N}{\partial z},z,t) \qquad . \tag{17}$$

515 We adopt the Keller-box method [Keller, 1971]. Let $a(z,t)\frac{\partial N}{\partial z} = b$, equation (17) is discretized as

516 follows:

$$a^n_{i-1/2} \cdot \frac{N^n_i - N^n_{i-1}}{\Delta z} = b^n_{i-1/2} \qquad ; \tag{18a}$$

517

$$\frac{N^n_{i-1/2} - N^{n-1}_{i-1/2}}{\Delta t} = \frac{b^{n-1/2}_i - b^{n-1/2}_{i-1}}{\Delta z} + f^{n-1/2}_{i-1/2} \qquad . \tag{18b}$$

518

519 The superscript and subscript here denote that the time step and altitude point, respectively. Let,

$$\frac{N^n_i + N^n_{i-1}}{2} = N^n_{i-1/2} \qquad , \qquad \frac{N^n_i + N^{n-1}_i}{2} = N^{n-1/2}_i \qquad ,$$

520

$$\frac{b^n_i + b^n_{i-1}}{2} = b^n_{i-1/2} \qquad , \qquad \frac{b^n_i + b^{n-1}_i}{2} = b^{n-1/2}_i \qquad ,$$

521

522 equations (18a) and (18b) then become

$$a^n_{i-1/2} \cdot \frac{N^n_i - N^n_{i-1}}{\Delta z} = \frac{b^n_i + b^n_{i-1}}{2} \qquad ; \tag{19a}$$

523

$$\frac{N^n_i + N^n_{i-1} - N^{n-1}_i - N^{n-1}_{i-1}}{2\Delta t} = \frac{b^n_i + b^{n-1}_i - b^n_{i-1} - b^{n-1}_{i-1}}{2\Delta z} + f^{n-1/2}_{i-1/2} \qquad . \tag{19b}$$

524

525 $\partial N/\partial z$ contained in the function f at half altitude grid i-1/2 is discretized using center difference.

526 The electron/ion temperature profiles contained in functions a and f are obtained from the energy

527 equations solved at the half time step n-1/2 and interpolated to half altitude grid points. After some

528 algebra equations (19a) and (19b) can be converted into a tridiagonal matrix form and solved

529 numerically. The continuity equations for O^+ and NO^+ are solved separately, while the coupling

530 term between them (the last term in equation 11) is treated via an iterative approach similar to that

531 dealing with the ion-electron coupling in their energy equations. The above numerical scheme is

532 found to be stable, as long as the diffusion coefficient $k(T_{i//} + T_e)/m_i\nu_i$ is not too large. In

533 practice, we limit the upper boundary at 500 km in solving the time-dependent ambipolar diffusion

534 equation of NO^+ and O^+ ions. This is due to both scientific and numerical considerations. We recall

535   that equations (9) and (10) are derived under a steady-state assumption and with the neglecting of

536   the advective term $(\mathbf{v} \cdot \nabla)\mathbf{v}$ in the momentum equations. At higher altitudes with an increasing

537   magnitude of ambipolar drifts, the above assumptions may become questionable. In SAID/STEVE

538   cases the ion upflows may reach a few km/s [e.g., Nishimura et al., 2020], i.e., be supersonic, in

539   the topside ionosphere, and the ion-ion collision also becomes important at those altitudes. Even

540   if we dismiss the above theoretical complication and adopt equation (9) anyway, the very large

541   diffusion coefficient and ambipolar drift speed at high altitudes impose a serious challenge to the

542   stability of the numeral scheme and considerably increase the computational cost. At last, we

543   emphasize again the main research interest of the current study is in the lower ionosphere (<200

544   km altitude). A more accurate description of the ionospheric variations and ion upflows in the

545   topside ionosphere under SAID would require a different model, probably involving the full

546   electron/ion momentum equations [e.g., Loranc and St-Maurice, 1994; Sydorenko and Rankin,

547   2013], which will be left for future studies.

548   Due to the above considerations, we run the time-dependent continuity equation up to 500 km

549   altitude, with the upper boundary condition specified by $u_{i//}$. The way we specify $u_{i//}$ at the

550   boundary is to be given in section 4.1 when we introduce the model run setup. Beyond 500 km

551   altitude, we continue to calculate the plasma density up to 800 km by assuming a flux conservation

552    $\frac{n_i u_{i//}}{B}$=const, corresponding to a steady-state ionosphere under ambipolar diffusion in the absence

553   of chemical production/loss. With such an assumption, equation (11) consists of coupled first-

554   order ODEs for NO^+ and O^+ densities, which are solved via a Runge-Kutta method starting from

555   500 km altitude. Extensive numerical tests have been performed and confirmed that, while the

556   uncertainty in the specification of the upper boundary condition for the ion continuity equation

557   would affect the solutions in the upper/topside ionosphere, the main research interest in this study,

558   namely the plasma dynamics in the lower ionosphere and the FAC variations (which is dominantly

559   accumulated in the lower ionosphere), is relatively insensitive to the upper boundary condition.

560   We solve the FAC via numerical integration,

561
$$j_{//}(z) = -B \cdot \int_{z_0}^{z} \frac{\nabla_\perp \cdot (\sum N_i \mathbf{u_{i\perp}})}{B \sin I} \cdot dz \qquad . \qquad (20)$$

562   The bottom boundary z_0 is set at 90 km. The integral is performed over field-aligned grids, and

563   we adopt the Newton-Cotes formula in the numerical integration [Press et al., 2007]. When $j_{//}$ is

564   evaluated in the topside ionosphere, equation (20) is equivalent to the well-known form of $-\nabla \cdot$

565   $(\Sigma_p \mathbf{E})$, in which Σ_P is the height-integrated (more precisely field-line-integrated) Pedersen

566   conductance. In this study, both Σ_P and FAC are evaluated up to the altitude of 500 km, i.e., the

567   nominal Swarm satellite altitude, to facilitate comparison with Swarm observations, the main data

568   source of SAID/STEVE to date.

569   Finally, we shall deal with the perturbation of electric fields due to the rise of the $E_{//}$ (see

570   equation 13). The electric potential perturbation is obtained via a numerical integral along the field

571   line from an upper boundary z_{top} ,

572
$$\delta\Phi = -\int_{z}^{z_{top}} \left(\frac{\mathbf{j}_{//}}{\sigma_{//}} - \frac{\nabla p_e}{N_e e} - \frac{m_e v_{en}}{N_e e} \sum N_i u_{i//} \right) \cdot \frac{dz}{\sin I} \qquad . \qquad (21)$$

573   The perturbed perpendicular electric field is then calculated via $\delta\mathbf{E}_\perp = -\nabla_\perp \delta\Phi$ and applied to

574   adjust the ion Pedersen drift and in turn the FAC. Iteration is made until convergent solutions of

575   $j_{//}$, $E_{//}$ and $\delta\Phi$ are reached at each timestep. z_{top} is set as 500 km altitude in our following run, where

576   the external SAID electric field is imposed. A boundary condition $\delta\Phi$=0 is assumed at 500 km

577   altitude. We have numerically tested with higher upper boundary altitudes of $\delta\Phi$, and find that

578   they produce virtually indiscernible difference to the result. More specifically, changing z_{top} from

579   500 km to 800 km would result in only ~1% difference to the final FAC outcome.

580

581   **3. Electron precipitation surrounding SAID/STEVE**

582   To simulate the ionospheric variations under SAID/STEVE, we first need to know the ambient

583   condition of the ionosphere surrounding SAID. SAID/STEVE is located in the nightside

584   subauroral region. However, ionization sources are not entirely absent there. First, even on the

585   nightside the geocorona scattering consistently provides weak ionization sources [Thomas, 1963].

586   Such nightside ionization sources are considered in our model using the same specification

587   embedded in the TIEGCM and GLOW models [Solomon, 2017]. More importantly, existing

588   observations of STEVE suggested that the electron precipitation is weak but not zero surrounding

589   STEVE. In the following we shall review two such observations in the existing literature, with

590   new datasets and aspects added. The first event was reported by Gallardo-Lacourt et al. [2018a].

591   Figure 2 shows the POES/NOAA satellite data. The upper panel gives the Total Electron detector

592   (TED) observations of the total electron precipitation fluxes in the whole TED energy range 50

593   eV-20 keV. It is key to notice that the STEVE arc is located amid a weak (<0.1 erg/cm^2/s) yet non-

594   zero electron precipitation region with increasing fluxes toward higher latitudes. The bottom panel

595   of Figure 2 shows the energy channel of the TED sensors where the differential electron fluxes

596   maximize, which is often used to evaluate the characteristic energy of the electron precipitation.

597   Such max-flux energy bins are found to be relatively stable at ~1-2 keV as the ionospheric footprint

598   of NOAA-17 traverses STEVE.

599   The other event was reported by Gillies et al. [2019]; their Figure 1 is copied as Figure 2b here.

600   In short, the authors sampled the Transition Region Explorer (TREx) spectrometer measurements

601   on STEVE and its surrounding neighbors. The optical spectrum of STEVE shows a continuous

602   enhancement over its ambient neighbors over a broad range of wavelengths, which constitutes the

603   main source of the STEVE brightness. Our interest here is focused on the small yet distinct peak

604   around 428 nm wavelength that exists in both STEVE and its ambient neighbors. This presumably

605   comes from the 427.8 nm blue-line emission of the N_2^+ 1NG system. Such an emission requires

606   ~19 eV excitation energy, and is thus generally recognized as a sign of auroral electron

607   precipitation. Similar 427.nm emissions are also observed in Liang et al [2019]'s STEVE event. It

608   is important to notice that the STEVE does not show appreciable enhancement over surrounding

609   neighbors in terms of the blue-line intensity, so that the 427.8 nm emissions constitute an ambient

610   background, instead of a characteristic emission line, of STEVE. To view the latitudinal profile of

611   the blue-line emission, we sample the meridional distribution of the 427.8 emission intensity

612   during 0640-0641 UT, when the STEVE was the brightest, from TREx spectrometer data. To

613   calculate the 427.8 nm emission intensity, we subtract the out-of-band spectral intensity, taken as

614   the average in 420-425 nm and 430-435 nm wavelength ranges, from the measured spectra, and

615   then integrate the subtracted spectral intensity in 425-430 nm range. Figure 2c shows the

616   distribution of the obtained 427.8 nm emissions versus MLAT. It is interesting to note that the

617   STEVE arc is located amid an increasing slope (toward north) of the blue-line intensity, which is

618   consistent with the POES/NOAA observation in the previous event.

619   The above inference that STEVE is located amid a region of weak yet increasing (toward high

620   latitudes) electron precipitation is compatible with some other existing observations. Based on

621   DMSP observations Burke et al. [2000], He et al. [2014] and Nishimura et al. [2020] all found that

622   the electron fluxes increase across SAID toward high latitudes. Vis optical data Yadav et al. [2021]

623   found that STEVE is embedded in a region with weak but increasing diffuse emissions toward

624 high latitudes. On the other hand, based on magnetospheric observations Chu et al. [2019] and

625 Nishimura et al. [2019] both noticed that the magnetospheric root of STEVE/SAID is situated in

626 a transition from the plasmapause into the electron plasma sheet, where electron fluxes increase

627 toward tail across the magnetospheric SAID structure. To summarize, existing observations invoke

628 the necessity of the inclusion of electron precipitation into the frame of a SAID model. This is

629 particularly important if one considers the current generator mechanism of SAID, which we shall

630 briefly discuss in Section 5. We emphasize again that the weak electron precipitation surrounding

631 STEVE cannot by itself directly account for the optical brightness of STEVE [Gillies et al., 2019],

632 but whether such weak precipitation may play certain indirect roles [e.g., Chu et al., 2019] in the

633 STEVE mechanism is a pending question to be examined in the future. We also admit that detailed

634 knowledge about the electron precipitation associated with STEVE and Picket Fence is still limited

635 (and to a certain degree controversial) to date, based upon unabundant events, so that our

636 specification of the precipitation profile is not without uncertainty in this study. The ambient

637 electron precipitation is embedded in our model as a necessary yet adjustable component.

638

639 **4. Model simulation**

640 We now present the model run and the results. We first clarify that, the current paper is mainly

641 intended to introduce our model and demonstrate a few key aspects and results from the new model.

642 We have made many test runs with different specifications and profiles of SAID as well as of the

643 ambient ionosphere, and are convinced that the main results and conclusion of this study are not

644 quantitatively changed. It is however inappropriate to elaborate all those test runs in the current

645 paper. In the interest of brevity we will be content, in this paper, to demonstrate three runs that use

646 typical SAID parameters, leaving for a separate publication a more comprehensive examination of

647　the subtlety of ionospheric dynamics, including certain neutral constituents that may potentially

648　contribute to STEVE, under different SAID and ambient ionospheric/precipitation conditions.

649　4.1 Model run setup

650　　The ambient and initial conditions of the subauroral ionosphere are set up as follows. We

651　assume a weak yet gradually increasing (from 0.02 to 0.06 erg/cm^2/s across SAID) ambient

652　electron precipitation. The precipitation flux spectrum is assumed to be Maxwellian with

653　characteristic energy of 2 keV. The above specification is partly based upon the realistic

654　observations in Gallardo‑Lacourt [2018a]. The Boltzmann transport of precipitating auroral

655　electrons is solved via a two-stream electron transport code [Banks, 1974; Solomon et al., 1988]

656　in our model. The plasma convection is initially set as zero, and the electron heat flow at the upper

657　boundary is initially set as a quiet-time value (2×10^9 eV/cm^2/s, e.g., Fallen and Watkins [2013]).

658　We start from the IRI-2016 model with parameters conformal to the realistic

659　geophysical/geomagnetic conditions in the 10 April, 2018 event [Gillies et al., 2019], and run our

660　model (without flow) to a chemical-diffusion equilibrium, which will be then used as the

661　initial/ambient condition of the subsequent run with SAID.

662　　The latitudinal profile of SAID plasma flows is as follows:

663
$$V_y = \begin{cases} 0 & x < -d \\ V_{y0}\cos^2\left(\frac{\pi x}{2d}\right) & -d < x < 0 \\ V_{y0}\left[\alpha + (1-\alpha)\cos^2\left(\frac{\pi x}{2d}\right)\right] & d > x > 0 \\ \alpha V_{y0} & x > d \end{cases} \tag{22}$$

664　in which V_{y0} denotes the peak SAID speed, and d controls the width of the SAID channel. The

665　flow profile is imposed at 500 km altitude. In the absence of $E_{//}$, which is deemed so in our initial

666　condition, the azimuthal convection flow maps along a field line according to $V_y(r) \propto r^{3/2}$ in which

667   r is the radial distance to the Earth's center. Note that in our specification there is a constant weaker

668   azimuthal flow, parametrized by a small α, poleward of SAID. This is motivated by the

669   observations that, in many realistic cases, weaker yet nontrivial westward plasma flows were often

670   found to exist immediately poleward of SAID, e.g., Anderson et al. [2001] (see their Figure 1),

671   Archer et al. [2019a] (panel a and b in their Figure 1), Nishimura et al. [2019] (see their Figure 3),

672   and Nishimura et al. [2020] (see their Figure 2). Clues of the existence of such westward flows

673   just poleward of STEVE may also be indirectly hinted from the neutral observations in Liang et

674   al. [2021]. Westward neutral winds were found to be strongly intensified ($\geq$200 m/s) at latitudes

675   higher than STEVE yet remain weak equatorward of STEVE. Upon a reasonable premise that the

676   neutral winds at subauroral latitudes are mainly driven by ion drag, one may infer the existence of

677   nontrivial westward plasma flows of several hundred m/s poleward of STEVE/SAID. The above

678   observations are also consistent with the fact that, during major substorm intervals SAPS-like

679   westward plasma flow enhancements are often found to exist equatorward of auroras and extend

680   to subauroral latitudes [Nishimura et al., 2009; Zou et al., 2012; Lyons et al., 2015]. In the

681   following run we set V_{y0} =4250 m/s, d =0.3^0 MLAT, and α=1/8. The peak SAID velocity is

682   selected here according to the median value of eight Swarm-STEVE conjunctive events in Archer

683   et al. [2019a] (see their Figure 2), and the width d is inferred form the mean half-peak-width of

684   SAID profiles shown in Archer et al. [2019a].

685   Our model has an electron heat flow as the boundary condition at 800 km altitude. Such a heat

686   flow is set to follow the function form $a + b\cos^2(\pi x/2d)$, with a peak of 2.8×10^{10} eV/cm^2/s at

687   the center (x=0) of SAID and a quiet-time value of 2×10^9 eV/cm^2/s outside SAID ($|x|>d$). The

688   external electron heat flow is so specified that it can reproduce the realistic T_e observations within

689   intense SAID in the topside ionosphere, as we shall elucidate in the following subsection. The

690 SAID and external heat flow are turned on at t=0, and we shall trace the time evolution of the

691 plasma temperature, density, and currents afterward.

692 The other boundary condition is the ion field-aligned drift at 500 km altitude. We assume $u_{i//}^{500}$

693 =0 for the ambient ionosphere run. For the SAID run, under the notion that the ion upflows in the

694 upper/topside ionosphere are driven by the frictional heating which, to the first order of

695 approximation, is proportional to V_y^2 [e.g., St-Maurice et al., 1999], we use a heuristic specification

696 for the ion upflows at 500 km altitude. $u_{i//}^{500} = \gamma \cdot V_y^2$. In our following model run the factor γ is

697 set as 3×10^{-5} s/m for O$^+$ and 2×10^{-5} s/m for NO$^+$. Their ratio 1.5 is set according to a rough

698 comparison of their $m_i \nu_{in}$ values in the topside ionosphere. The peak O$^+$ and NO+ upflow speeds

699 are thus ~540 m/s and ~ 360 m/s in the center SAID at 500 km altitude in our model run.

700 As afore-mentioned, existing STEVE observations indicate that its azimuthal extension may

701 span over ~2.5h MLT sectors [Gallardo-Lacourt et al., 2018b; Nishimura et al., 2020]. Assuming

702 this represents the azimuthal scale of a SAID segment, a 4250 km/s (at 500 km altitude) SAID

703 flows would have a lifetime of ~9 min in the SAID segment. In other words, any new plasma fed

704 into the SAID channel by the ambient global convection has a duration of no more than ~10 min

705 to undergo SAID-imposed changes, even though the SAID itself may last longer. In practical in-

706 situ observations, contingent upon the relative location of the satellite in the SAID segment, the

707 interaction time between the new plasma's SAID entry and its detection by the satellite is typically

708 limited to several minutes. Certainly, such an interaction time is flow-velocity dependent, and is

709 longer at the edge of the SAID channel. Based on the above considerations, we set the maximum

710 simulation time at latitude x to be 18 min or $L_0/V_y(x)$, whichever is smaller. L_0 is set as 2.5 h MLT,

711   and $V_y(x)$ comes from our SAID profile specification (19). For $t > L_0/V_y(x)$, the ionospheric

712   profiles at the corresponding latitude are deemed to be no longer time-varying.

713   4.2 Simulation results

714   Movies showing the full time evolution of T_e, T_i, N_e, and **j**, are given in supplementary

715   material. The latitudinal profiles of SAID and the background precipitation are plotted on top for

716   reference. It should be noted that the height profile presented in all movies and subsequent figures

717   actually represents the altitudinal distribution along a magnetic field line. Figures 3 to 5 exemplify

718   the T_e, T_i, and N_e profiles, respectively, at t=0, 30 sec, 2 min, 5 min, 10 min, and 15 min. As one

719   can see from the movie, T_e increases rapidly in the E-region right after the onset of SAID, which

720   indicates the AEH effect. Later on, T_e also increases in the upper F-region, and appears to follow

721   a two-step evolution: first a rapid yet weaker enhancement over a broad range of altitudes, then a

722   stronger yet more gradual enhancement that shows a downward propagation trend from the topside

723   ionosphere. Such a T_e enhancement in the upper F-region is led by heat flux conduction from the

724   topside ionosphere [e.g., Rees and Roble, 1975; Moffett et al. 1998]. As afore-mentioned, when

725   considering the finite azimuthal extension of SAID, contingent upon the azimuthal location of the

726   satellite passage, the plasma captured by the satellite at the peak flow latitude usually undergoes

727   SAID intensification for no more than several minutes. Our simulation indicates that, at t=5 min,

728   the peak T_e at the center latitude of SAID reaches ~7500 K at 500 km altitude, close to the median

729   value of peak T_e enhancements under SAID as reported in Archer et al. [2019a].

730   As to the ion temperature, T_i dramatically increases due to ion frictional heating. The

731   enhancement first occurs in the lower ionosphere, and quickly expands to higher altitudes. Overall,

732   SAID leads to intense ion frictional heating over a broad range of altitudes. There is a slight

733   decrease of T_i at >300 km altitude after ~2 min, which is due to the adiabatic cooling associated

734 with ion upflows [Wang et al., 2012]. T_i reaches ~16000 K in the lower ionosphere at the center

735 of SAID in our simulation, which is compatible with existing theories and simulations of frictional

736 heating. Assuming a balance between the ion frictional heating and the collisional cooling with

737 neutrals, a simple equation of ion temperature can be written as $T_i = T_n + \frac{\langle m_n \rangle}{3k} V_i^2$ [e.g., St-

738 Maurice et al., 1999], in which $\langle m_n \rangle$ denotes the collision-frequency-weighted averaged neutral

739 mass. In the lower ionosphere where N_2 is the major neutral constituent, $V_E \sim 4$ km/s would lead

740 to ~18000 K ion temperature according to the above theory. Moffett et al. [1998] also predicted T_i

741 up to ~15000 K in a numerical simulation of SAID with V_E=4 km/s. In an event with T_i

742 measurement onboard DE-2 satellite, Anderson et al. [1991] (see their Figure 1) found that T_i at

743 ~388 km altitude exceeded 10000 K when the SAID V_y reached ~4 km/s. Notwithstanding the

744 uncertainty in T_i measurements by ISR [Akbari et al.; 2017; Goodwin et al., 2018], St-Maurice et

745 al. [1999] reported a case in which T_i obtained from EISCAT observations (though closer to $T_{i//}$

746 under their radar geometry) exceeded 10000 K in the lower F-region when the convective electric

747 field temporarily reached ~225 mV/m.

748 　　We turn next to the plasma density variations under SAID. As one can see from the movie,

749 after the start of SAID, N_e in the E- and lower F-region begins to increase in the poleward portion

750 of the SAID channel and to decrease in the equatorward portion of SAID. As time evolves the

751 equatorward density depletion slowly propagates a bit poleward into the center of SAID, as well

752 as extends upward to higher altitudes. These variations are led by the transport term $\nabla \cdot \left(N_i \boldsymbol{u}_{pi} \right)$

753 in the continuity equation. More specifically, $N_i \nabla \cdot \boldsymbol{u}_{pi}$ and $\nabla N_i \cdot \boldsymbol{u}_{pi}$ are both depletion terms in

754 the equatorward side of the SAID channel. With growing density variations the $\nabla N_i \cdot \boldsymbol{u}_{pi}$ term

755 gradually drives the density depletion to the poleward side of SAID (except at the very edge of

756 SAID where the $N_i \nabla \cdot \boldsymbol{u}_{pi}$ term leads to a pileup) as well as upward to higher altitudes, conformal

757　to the $\boldsymbol{u}_{pi}$ direction under a tilted field-line geometry. The role of ion Pedersen drift in depleting

758　the lower ionosphere was initially addressed by Banks and Yasuhara [1978]. The plasma density

759　variation in the lower ionosphere shows the most dynamic change in the first couple of minutes,

760　yet becomes slowly changing and/or relatively stable afterward.

761　　To better highlight the role of ion Pedersen transport in density variations, it is instructive to

762　compare with the simulation without the ion Pedersen drift, even though the latter simulation may

763　be scientifically problematic for the SAID phenomenon of intertest. In Figure 6, we plot side-by-

764　side the T_e and N_e profiles at t=10 min with ion Pedersen drift (leftside) and artificially without ion

765　Pedersen drift (rightside). All other model parameters are the same. There is little difference in T_e

766　between the two runs, but their N_e profiles in the lower ionosphere differ dramatically. Compared

767　to the initial condition (t=0 in Figure 5), N_e noticeably increases within SAID between ~100-120

768　km altitude in the simulation run without ion Pedersen drift. This is consistent with the simulation

769　results in Noel et al. [2005], Milikh et al. [2006], and Liu et al. [2016], all of which did not consider

770　the ion Pedersen drift. Such a plasma density enhancement is due to the decrease of the

771　recombination rate of NO^+ under enhanced T_e in the AEH region. The dramatic difference in N_e

772　between the two runs naturally leads to difference in Σ_p (bottom panels of Figure 6): Σ_p decreases

773　in a major portion of SAID when the ion Pedersen drift is included, yet increases within SAID if

774　the ion Pedersen drift is not considered [e.g., Liu et al., 2016]. The neglect of ion Pedersen drift

775　might be acceptable for electric field enhancement structures with much larger spatial width and

776　weaker strength (such as SAPS). However, for the intense SAID of our interest, when the ion

777　Pedersen drift and the narrow width of the SAID channel are considered, the transport effect led

778　by the ion Pedersen drift and its divergence/convergence dominates over the chemical

779　recombination process in terms of their contributions to density variations in the lower ionosphere.

780 As we have mentioned in section 2.1, with their Pedersen drift the E-region ions typically traverse

781 the SAID channel in several tens of seconds, while the recombination of NO^+ is much slower due

782 to reduced rate coefficient under high T_e [Parlov, 2014]. The rapid density depletion in the lower

783 ionosphere is almost purely led by the ion Pedersen transport effect. We note that density depletion

784 due to ion Pedersen transport was also reported in Zettergren and Semeter [2012]. In conclusion,

785 we emphasize that the ion Pedersen drift plays a pivotal role in the density variation in the lower

786 ionosphere under SAID, and should be taken into consideration in ionospheric models of SAID.

787 The plasma density variations in the upper ionosphere where the ion Pedersen drift vanishes

788 are driven by fundamentally different processes. One well-recognized mechanism of such a plasma

789 depletion in the F-region ionosphere is a conversion from O^+ to NO^+ ions via the reaction,

$$O^+ + N_2 \rightarrow NO^+ + N \qquad , \qquad (R1)$$
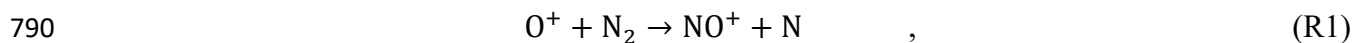
791 whose reaction rate increases rapidly with enhanced ion temperature and electron temperature [St-

792 Maurice and Laneville; 1998, Moffet et al., 1992b; 1998], causing NO^+ to replace O^+ to become

793 the major ion species in the F-region under strong SAID. Since NO^+ has a faster recombination

794 rate than O^+ --- this is true even under elevated T_e --- the plasma density decreases accordingly.

795 However, it should be noted that such a chemistry-driven density depletion does not work

796 effectively in the lower ionosphere where NO^+ is inherently the dominant ion species. The other

797 important process contributing to the plasma density variations in the upper/topside ionosphere is

798 the ion upflows [Anderson et al., 1991; 1993]. As one can see from the movie and Figure 5, there

799 is a gradual decrease of the F-region peak density at ~300-350 km, which is primarily led by the

800 above-depicted reaction R1. Above 400 km, the density is temporarily enhanced during the first

801 minute, which is driven by the thermal expansion of plasma via upflows under elevated

802 temperature. Later on, as the plasma density continues to drop in the entire F-region, notable

803   density depletion throughout the upper ionosphere becomes evident around the center of SAID

804   after ~2 min, and gradually deepens with time. Schunk et al. [1976] modeled the generation of

805   electron trough in the nighttime F-region. Though they did not include the ion Pedersen drift effect

806   and only qualitatively discussed the role of vibrationally-excited N_2 in their study, they reached a

807   similar conclusion to ours that the reaction (R1) under enhanced electric field and ion upflows

808   constitute the two main mechanisms contributing to the density depletion in the upper F-region.

809   Figure 7 demonstrates the altitudinal profile of the densities of N_e, NO^+ , and O^+ at the center

810   (x=0) of SAID at t=0, 1 min, and 5 min, and 10 min. Initially, NO^+ is the dominant ion species in

811   the lower ionosphere, while O^+ is dominant at >250 km height. At t=1 min, NO+ density is

812   enhanced substantially and starts to exceed the O^+ density in the F-region ionosphere due to the

813   reaction R1. The O^+ density continues to drop significantly in the entire upper ionosphere due to a

814   combined effect of the chemical process and the upflow evacuation [Anderson et al., 1991; 1993],

815   and NO^+ becomes the major ion species there, though its density also drops with time in the upper

816   ionosphere due to recombination and upflows. The simulation results predict that N_e in the

817   upper/topside ionosphere would drop to the order of a few 10^3 cm^{-3} at the center of SAID,

818   compatible with existing observations [Archer et al., 2019a; Nishimura et al., 2019; 2020].

819   Figure 8 shows the altitudinal profile of the Pedersen conductivity at the center of SAID at

820   t=30 sec, 2 min, 5 min, and 10 min. The initial Pedersen conductivity (t=0) is overplotted in a

821   dotted line for reference. Due to the density depletion, the Pedersen conductivity decreases at

822   almost all altitudes of interest, but the conductivity peak is always confined to the lower ionosphere.

823   In terms of the height-integrated Pedersen conductance Σ_P, most of the contributions would come

824   from the lower ionosphere. Movies showing the full time evolution of the MLAT-altitude

825   distribution of the current vectors, as well as of the Σ_P and FAC at 500 km altitude, are given in

826   supplementary material. We demonstrate the latitudinal profiles of Σ_P and FAC at t=0, 30 sec, 2

827   min, 5 min, and 15 min in Figure 9. Quickly following the start of SAID, Σ_P decreases significantly

828   and drops to very low levels (~0.1 S) in the equatorward and center portion of SAID, yet increases

829   at the poleward edge of SAID. Banks and Yasuhara [1978] reported a similar change of Σ_P in their

830   model. The FAC is initially large upon the incidence of SAID, but quickly decreases in magnitude

831   due to the reduction of Σ_P. We further note that the change of Σ_P and FAC is dynamic in the first

832   2 minutes elapsed time, but becomes slowly varying after that time and even quasi-stable after ~5

833   min. This indicates that the conductance drop comes more from the Pedersen-transport-driven

834   density depletion in the lower ionosphere than from the gradual density depletion in the upper

835   ionosphere driven by chemical processes and upflows. When reaching a quasi-steady state, the

836   simulated FAC in a main portion of SAID is downward with magnitude smaller than and/or close

837   to ~1 $\mu A/m^2$ or, compatible with observations [Archer et al., 2019a; Chu et al., 2019; Nishimura

838   et al., 2019; 2020]. We have also made other test runs with stronger SAID V_y magnitude, and

839   noticed that the steady-state downward FAC level is relatively insensitive to the peak flow

840   magnitude. The reason is that, with stronger SAID the ion Pedersen drift is also enhanced, leading

841   to a deeper density depletion in the lower ionosphere and the reduction of Pedersen conductance,

842   so that the FAC level remains more or less the same.

843   On the other hand, a stronger upward FAC appears at the poleward edge of the SAID channel.

844   We note that many existing proposals of the generation mechanism of SAID postulated the

845   existence of upward FACs at the poleward edge of SAID [e.g., Anderson et al., 1993; 2001; De

846   Keyser et al., 1998]. Such upward FACs were indeed observed near the edge of SAID, and are

847   deemed as related to the Picket Fence phenomenon [Nishimura et al., 2019], though their observed

848   intensity (<1 $\mu A/m^2$) tends to be weaker than that in our simulation (peak at ~2 $\mu A/m^2$). Chu et al.

849   [2019] reported an event (see their Figure 2) that an upward FAC peaked at ~1.2 μA/m^2 at the

850   poleward edge of SAID. We shall recall that the number of existing events under intense SAID

851   condition and with in-situ FAC measurements remains limited to date, and that the technique to

852   derive FAC density from single-satellite magnetic field measurements relies on a current sheet

853   assumption, whose credibility in the case of small-scale FAC structures is questionable [Forsyth

854   et al., 2017]. The latitudinal scale of the upward FACs in our simulation is <10 km, which is

855   marginal for the single-satellite FAC technique. For reference, existing FAC observations under

856   intense SAID came predominantly from DMSP and Swarm 1 Hz magnetic field data, both of which

857   have a spatial resolution of ~8 km. It is thus not impossible that the existing FAC observations

858   based on single-satellite measurements tend to underestimate the peak upward FAC density. Using

859   high-resolution (50 Hz) Swarm magnetic field data, Nishimura et al. [2019] obtained a much larger

860   FAC density (up to ~10 μA/m^2 spike, see their Figure 2), though the accuracy of the FAC

861   determination at this temporal/spatial scale may be questionable [Forsyth et al., 2017].

862   The discrepancy between the simulated upward FAC intensity and the realistic observations

863   may also result from uncertainties in our model parameters. Since the upward FAC is contributed

864   by the convergence between the Pedersen current inside the poleward edge of the SAID and that

865   outside the SAID, the overestimation of upward FACs may be relieved in two ways: by adjusting

866   the flow gradient and level surrounding the poleward edge of SAID, and/or by adjusting the

867   ambient Pederson conductance surrounding the poleward edge of SAID. In this paper we only

868   demonstrate the former possibility. In the previous run we assumed an azimuthal convection flow

869   (V_y) of 1/8 the peak SAID speed, or ~530 m/s in practice, poleward of the SAID channel. In the

870   following run, we assume a higher constant V_y flow of 850 m/s (α=1/5 in equation 22) poleward

871   of SAID. Note that a change of V_y flow poleward of SAID is equivalent to a change of the ion

872   Pedersen drift out of SAID. Figure 10 displays the altitude-latitude distribution of N_e and the

873   latitudinal profile of FAC at t=15 min from the new run. The density depletion in the equatorward

874   and center portion of SAID seems not to be notably affected by the change in V_y level poleward of

875   SAID, but the density enhancement and FAC at the poleward edge of SAID become substantially

876   weaker than those in the previous run. The peak upward FAC at the poleward edge of SAID is

877   now limited to <1 $\mu A/m^2$. Vice versa, we have also tested the case that the flow magnitude is

878   reduced to zero poleward of STEVE, and found that the resulting upward FAC density rises

879   significantly (peak at ~4.5 $\mu A/m^2$, not shown). We thus infer that the upward FAC level is fairly

880   sensitive to the flow condition surrounding the poleward edge of SAID; a moderate relaxing

881   (steepening) of the attenuation edge of SAID would cause a substantial decrease (increase) of

882   upward FAC density there. This shall not be unexpected. A smoother V_y gradient around the edge

883   of SAID imposes double-fold effects on the FAC: in addition to weaker convergence of electric

884   fields, a smoother change of V_y also leads to weaker convergence of ion Pedersen drifts and thus

885   less density buildup, and in turn smaller Σ_P. The FAC is thus expected to vary nonlinearly with the

886   V_y gradient. Some other possible reasons for the discrepancy between our simulated upward FAC

887   intensity and the realistic observations will be discussed in Section 5.

888   Our model contains a few external boundary conditions, and the modeled plasma density and

889   temperature in the upper/topside ionosphere are contingent upon the upper boundary conditions

890   such as the external heat flow and the ion upflows. However, the lower ionosphere plasma

891   parameters and FAC variations are found not to be sensitive to these upper boundary conditions.

892   To exemplify this, we demonstrate a test run in which the upper boundary heat flux is set constant

893   at the background level (2×10^9 eV/cm^2/s), i.e., there is no extra heat flux input associated with

894   SAID. All other parameters and boundary conditions are the same as the first run described

895   previously. The new run results are plotted on the right-side of Figure 11, to facilitate a side-by-

896   side comparison with the results in the first run with extra heat flux, which are plotted on the left-

897   side. Though without extra heat flux input, T_e in the upper ionosphere still slightly increases over

898   background within SAID due to the decrease in plasma density there. However, the level of T_e

899   enhancement in the new run is substantially lower than the realistic T_e observation under STEVE-

900   related SAIDs [Archer et al., 2019a, Nishimura et al., 2019]. This implies that external heat flux

901   is likely required to account for the extreme electron heating in realistic observations, consistent

902   with the conclusion in Moffett et al. [1998]. On the other hand, lower T_e in the upper ionosphere

903   leads to smaller vibrationally excited N_2 population and in turn slower conversion rate from O^+ to

904   NO^+, so that the plasma density in the upper ionosphere in the new run is noticeably larger than

905   that in the previous run, even though we have used the same upflow boundary condition. It is

906   important to note that, in contrast to the large difference in the upper ionosphere, the lower

907   ionosphere (<200 km) of our main interest in this study shows much smaller, or even indiscernible,

908   differences between the two runs. The FACs (calculated at 500 km altitude) in the two runs are

909   very similar to each other, because the FAC is dominantly accumulated in the lower ionosphere

910   by divergence/convergence of Pedersen currents there. The above comparison clearly shows that,

911   the lower ionospheric variations and FACs are insensitive to the imposed heat flux at the upper

912   boundary, since they are mainly driven by the ion Pedersen transport effect across the SAID

913   channel. We have also tested with a variety of ion upflows at the upper boundary (not shown) and

914   achieved a similar conclusion.

915

916   **5. Discussion**

To date, existing observations and model simulations of SAID-related ionospheric variations have been focused on the upper F-region and topside ionosphere, yet the variations and structures in the E-region and lower F-region ionosphere led by SAID remain largely unexplored. In this study, we present a time-dependent 2D model simulation of self-consistent variations of the electron/ion temperature, density, and FAC, under strong SAID, with main focus in the lower ionosphere. In particular, the ion Pedersen drift and its resultant density and FAC variations are self-consistently incorporated into the model. While some uncertainties admittedly exist due to insufficient observations to date, we have made decent attempts to evaluate the AEH and the ambient precipitation conditions surrounding SAID/STEVE based upon current understanding and available observations. Therefore, we have the ground to believe that our model represents the best effort to date in simulating the dynamic variations and structures in the lower ionosphere under intense SAID. While direct observations of the lower ionospheric variations under SAID are still lacking to date, we expect that some of our model results may be validated by the incoming EISCAT3D observations (to be fully operational in 2022).

Our simulation reproduces many key features of SAID that are consistent with the realistic observations and/or theoretical expectations, such as strong electron temperature enhancement in the upper F-region, intense ion frictional heating, and density depletion in the upper F-region. Most importantly, we highlight the key role of ion Pedersen drifts in the variations of the plasma density, the ionospheric conductance, and the FAC. Existing in-situ FAC observations under intense SAID often allude to much reduced Pedersen conductance within the SAID channel. We confirm in this study that a significant reduction of ionospheric conductance indeed occurs within SAID. Such a reduction of ionospheric conductance is mainly owing to the plasma density depletion in the lower ionosphere led by the transport effect associated with the ion Pedersen drift [Banks and Yasuhara,

940   1978], rather than driven by chemical processes, as the recombination is slowed down due to the

941   elevated electron temperature. The simulated FAC inside SAID is mainly downward with

942   magnitude $\leq \sim 1\ \mu A/m^2$, compatible with observations, though a stronger upward FAC exists at the

943   poleward edge of SAID.

944   Our model is based on an electrostatic approach. In our model run the SAID V_y profile is

945   externally specified, and is thus more aligned with the view of a voltage driver of SAID. The exact

946   formation mechanism of SAID is not entirely clear to date. The idea of the SAID mechanism being

947   associated with a magnetospheric source acting either as a voltage or as a current generator has

948   been a subject of discussion [Burke et al., 2000; Figueiredo et al., 2004; Mishin et al., 2017;

949   Maruyama, 2020]. Readers are referred to, e.g., Figueiredo et al. [2004] for a detailed discussion

950   in this regard and arguments for the co-existence of both voltage and current drivers. A full

951   electromagnetic approach would be more rigorous and desirable when the current driver nature of

952   SAID is considered. It is conceivable that the spatiotemporal evolution of the ionosphere

953   parameters in a current driver scenario under an electromagnetic approach might be different from

954   what is presented in this paper, though the essence of underlying physics, namely that the E-field

955   and FAC should evolve self-consistently with the evolving ionospheric state, would not change.

956   With the limitation of our current model assumption (voltage driver) and approach (electrostatic)

957   in mind, we stress that the present study aims to investigate the ionospheric variations under an

958   established SAID, instead of the generation mechanism of SAID. As far as an electrostatic steady-

959   state is concerned, our model yields valid solutions of the final levels of FAC and E-field, as well

960   as the ionospheric state. Furthermore, our model results unveil the crucial role of ion Pedersen

961   transport in the variations of the lower ionospheric density and the conductance: Σ_P is strongly

962   modified by SAID E-fields and is substantially reduced in a main portion of the SAID channel.

963 The basic physics would remain operative under a current driver scenario with evolving E-fields:

964 ion Pedersen transport would follow the intensifying E-fields and modify the plasma density and

965 Σ_P in a way similar to that in our model. This would lead Σ_P to decrease in a certain part of the

966 system, and in turn summon stronger E-fields there which further reduce Σ_P. Such positive

967 feedback would be the key for localized intense E-fields to develop under moderate FAC inputs.

968 To summarize, our study indicates that the ion Pedersen transport and its resultant

969 density/conductance variations should be taken into account in any SAID model involving self-

970 consistent evolution of E-field and FAC, no matter which one is deemed the main driver.

971 Looking forward, we are indeed working towards incorporating the current driver scenario of

972 SAID in a future version of our model. While the downward FAC is carried by proton precipitation

973 and/or outflowing ionospheric electrons, the upward FACs, from a current continuity perspective,

974 should be largely conformal to the suprathermal electron precipitation on top of the ionosphere.

975 As addressed in Section 3, existing observations indicated the presence of electron precipitation

976 surrounding STEVE, particularly in its poleward vicinity (see e.g., Nishimura et al. [2019; 2020]),

977 but the FAC carried by such precipitation is lower than the upward FAC density obtained in our

978 simulation. Via numerical tests, we found that the upward FAC level strongly depends on the V_y

979 gradients at the poleward edge of SAID. To match the observed upward FAC densities, a larger

980 flow magnitude immediately poleward of SAID is needed. This, from a current generator

981 perspective, can be rephrased in a way that the moderate upward FAC modifies the ionospheric

982 convection and result in a smoother flow gradient at the poleward edge of SAID. A refinement of

983 our model to accommodate the possible involvement of a current generator, particularly regarding

984 the upward FAC carried by electron precipitation at the poleward edge of SAID, is currently under

985 way and shall be the content of a separate publication in a near future.

986   Our simulation results indicate the presence of strong latitudinal gradients of plasma density,

987   temperature, and flows, at the edge of SAID. Figure 12 shows the latitudinal profiles of plasma

988   flows, T_e, T_i, and N_e , averaged over 100-150 km altitudes. As one can see, strong gradients of

989   plasma density, temperature, and flows exist at the edge of SAID. It is interesting to note that the

990   density gradients are stronger at the poleward side of SAID than at the equatorward side. Such

991   density/temperature/flow gradients are hotbeds of a number of plasma instabilities (see Kelley

992   [2009] for a thorough discussion of potential plasma instabilities in the ionosphere). For example,

993   the temperature gradient and density gradient are strong and oppositely directed at ~0.1-0.25^0

994   poleward of SAID, which is known to be conducive to the temperature gradient drift instability

995   [e.g., Hudson and Kelley, 1976]. Such temperature/density gradients are of course contingent upon

996   the actual SAID profile, and it is not impossible that in some cases the gradients can be even

997   steeper than that presented in our simulation with 0.025^0 MLAT grid resolution. These instabilities

998   may become an intrinsic part of the plasma dynamics at the poleward edge of SAID. We speculate

999   that those instabilities, when well developed, can reach a level that may have macroscopic effects

1000   on the plasma distributions and variations. For example, the instabilities at a nonlinear stage may

1001   lead to the presence of nonlinear currents ($e\langle \delta N_e \cdot (\delta V_i - \delta V_e)\rangle$), and in turn modify the local FAC

1002   configuration [e.g., Dimant and Oppenheim, 2011], which constitute another possible reason for

1003   the discrepancy between our modeled and observed FAC intensity at the poleward edge of SAID.

1004   The potential operation of instabilities in the presence of sharp plasma gradients in the lower

1005   ionosphere may have particular importance to the Picket Fence phenomenon. Picket Fence occurs

1006   at ~100-120 km altitude and is typically found at the poleward edge of STEVE [Semeter et al.,

1007   2020; Gillies et al., 2020]. It is dominated by green-line emission (excitation energy 4.19 eV) and

1008   also contains some N_2 1PG emissions (7.35 eV), but lacks the blue-line emissions (18.75 eV)

1009 [Gillies et al., 2019; Mende et al., 2019]. Clues of electron precipitation were found in association

1010 with Picket Fence [Nishimura et al., 2019], but the precipitation fluxes tend to be too weak to

1011 directly account for the optical brightness of Picket Fence. A number of researchers suggested the

1012 possibility that Picket Fence be generated by suprathermal electrons ($\leq \sim 10$eV) locally accelerated

1013 in the lower ionosphere [Mende et al., 2019; Gillies et al., 2020; Semeter et al., 2020]. However,

1014 the underlying mechanisms of such local acceleration remain elusive to date. Semeter et al. [2020]

1015 suggested that such electron heating mechanisms might be intrinsically related to certain local

1016 plasma instabilities at play in the lower ionosphere near the boundary of SAID, in concert with our

1017 above proposal. A dedicated exploration of the possible plasma instabilities is beyond the scope

1018 of the current paper and shall be left to future studies. Nevertheless, our results in this study have

1019 laid the foundation to, and prepared a quantitative context for, such an exploration in the future.

1020

1021 **6. Summary and conclusion**

1022 While it is now established that the STEVE and Picket Fence phenomena are inherently related

1023 to SAID, existing observations and models related to SAID have been limited to the upper F-

1024 region/topside ionosphere. The lack of definite knowledge of the lower ionospheric dynamics

1025 under intense SAID hampers the exploration of the underlying mechanism of STEVE and Picket

1026 Fence. In this study, we present a 2D time-dependent model simulation of the self-consistent

1027 variations of the electron/ion temperature, density, and FAC, under strong SAID, with main focus

1028 in the lower ionosphere. The E-region electron temperature enhancement led by AEH is evaluated

1029 using an observation-based empirical model [St-Maurice and Goodwin, 2021]. We reproduce

1030 many known or expected features of SAID, such as strong electron temperature enhancement in

1031 the upper F-region, intense ion frictional heating, and plasma density depletion. Most importantly,

the inclusion of ion Pedersen drifts is proved to be crucial to the density variations and FAC

dynamics in the lower ionosphere. We find that the ionospheric conductance is significantly

reduced within SAID, and indicate that the conductance reduction is mainly owing to the plasma

density depletion in the lower ionosphere, which is primarily driven by the transport effect of ion

Pedersen drifts instead of chemical effects. The simulated FAC inside SAID is mainly downward

with magnitude $\leq\sim1$ $\mu A/m^2$, in line with existing observations. Our simulation also predicts that

the plasma density in the lower ionosphere and in turn the Pedersen conductance increase at the

poleward edge of the SAID channel, leading to an upward FAC there that is qualitatively consistent

with, but tends to be somehow larger than, the realistic observations. Via numerical tests, we note

that this upward FAC is sensitive to the flow condition surrounding the poleward edge of SAID.

Given the potential limitation (e.g., a current-sheet approximation and latitudinal resolution) of the

FAC data drawn from in-situ observations, a moderate discrepancy between the model simulation

and the realistic FAC observations should not be deemed unreasonable, though we cannot exclude

the possibility that the discrepancy stems from certain limitations of our current model.

One other key aspect of this study is that, our simulation results corroborate the presence of

strong gradients of plasma density, temperature, and flows, at the edge of SAID. These gradients

are potentially conducive to a number of plasma instabilities. The potential operation of

instabilities in the presence of sharp plasma gradients in the lower ionosphere may have particular

importance to the Picket Fence phenomena, which are usually found near the poleward edge of

STEVE. The simulation results of the plasma dynamics and structures under SAID achieved in

this study establish the context of, and pave the road to, a future investigation of the possible

plasma instabilities at the edge of a SAID channel, our next-step task to carry on this study.

References.

Akbari, H., Goodwin, L. V., Swoboda, J., St.-Maurice, J.-P., and Semeter, J. L. (2017), Extreme plasma convection and frictional heating of the ionosphere: ISR observations, *J. Geophys. Res. Space Physics*, 122, 7581– 7598, doi:10.1002/2017JA023916.

Anderson, P. C., Heelis, R. A., and Hanson, W. B. (1991), The ionospheric signatures of rapid subauroral ion drifts, *J. Geophys. Res.*, 96(A4), 5785– 5792, doi:10.1029/90JA02651.

Anderson, P. C., D. L. Carpenter, K. Tsuruda, T. Mukai, and F. J. Rich (2001), Multisatellite observations of rapid subauroral ion drifts (SAID), J. Geophys. Res., 106(A12), 29,585–29,599, doi:10.1029/2001JA000128.

Anderson, P. C., W. B. Hanson, R. A. Heelis, J. D. Craven, D. N. Baker, and L. A. Frank (1993), A proposed production model of rapid subauroral ion drifts and their relationship to substorm evolution, J. Geophys. Res., 98(A4), 6069–6078, doi:10.1029/92JA01975.

Archer, W. E., & Knudsen, D. J. (2018). Distinguishing subauroral ion drifts from Birkeland current boundary flows. *Journal of Geophysical Research: Space Physics*, 123, 819– 826.

1074   Archer, W. E., Gallardo-Lacourt, B., Perry, G. W., St.-Maurice, J.-P., Buchert, S. C., & Donovan,

1075   E. F. (2019a). Steve: The optical signature of intense subauroral ion drifts. *Geophysical*

1076   *Research Letters*, 46, 6279– 6286. https://doi.org/10.1029/2019GL082687

1077   Archer, W. E., St.- Maurice, J.-P., Gallardo-Lacourt, B. (2019b). The vertical distribution of the

1078   optical emissions of a Steve and Picket Fence event. *Geophysical Research Letters*, 46,

1079   10719– 10725, https://doi.org/10.1029 /2019GL084473

1080   Baker, K. B. and S. Wing (1989), A new magnetic coordinate system for conjugate studies at high

1081   latitudes, *J. Geophys. Res., 94*(a7), p. 9139, doi:10.1029/JA094iA07p09139.

1082   Bahcivan, H. (2007), Plasma wave heating during extreme electric fields in the high latitude E

1083   region, Geophysical Research Letters, 34 (15). https://doi.org/10.1029/2006GL029236

1084   Banks, P. M., C. R. Chappell, and A. F. Nagy (1974), A new model for the interaction of auroral

1085   electrons with the atmosphere: Spectral degradation, backscatter, optical emission, and

1086   ionization, J. Geophys. Res.,79(10), 1459–1470, doi:10.1029/JA079i010p01459.

1087   Banks, P.M. and Yasuhara, F. (1978), Electric fields and conductivity in the nighttime E-region:

1088   A new magnetosphere-ionosphere-atmosphere coupling effect. Geophys. Res. Lett., 5: 1047-

1089   1050. https://doi.org/10.1029/GL005i012p01047

1090   Burke, W. J., Rubin, A. G., Maynard, N. C., Gentile, L. C., Sultan, P. J., Rich, F. J., de La

1091   Beaujardière, O., Huang, C. Y., and Wilson, G. R. (2000), Ionospheric disturbances observed

1092   by DMSP at middle to low latitudes during the magnetic storm of June 4–6, 1991, J. Geophys.

1093   Res., 105(A8), 18391– 18405, doi:10.1029/1999JA000188.

1094   Campbell, L., D. C. Cartwright, M. J. Brunger, and P. J. O. Teubner (2006), Role of electronic

1095   excited N_2 in vibrational excitation of the N_2 ground state at high latitudes, *J. Geophys.*

1096   *Res.*, **111**, A09317, doi:10.1029/2005JA011292.

1097   Cartwright, D. C., M. J. Brunger, L. Campbell, B. Mojarrabi, and P. J. O. Teubner (2000), Nitric

1098   oxide excited under auroral conditions: Excited state densities and band emissions, J. Geophys.

1099   Res., 105, 20,857 –20,867.

1100   Chu, X., Malaspina, D., Gallardo-Lacourt, B., Liang, J., et al (2019). Identifying STEVE's

1101   magnetospheric driver using conjugate observations in the magnetosphere and on the

1102   ground. *Geophysical Research Letters*, 46.https://doi.org/10.1029/ 2019GL082789.

1103   deBoer, J. D., J.‐M. A. Noël, and J.-P. St-Maurice (2010), The effects of mesoscale regions of

1104   precipitation on the ionospheric dynamics, electrodynamics and electron density in the presence

1105   of strong ambient electric fields, Ann. Geophys., 28, 1345– 1360, doi:10.5194/angeo-28-1345-

1106   2010.

1107   Dimant, Y. S., and G. Milikh (2003), Model of anomalous electron heating in the E region: 1.

1108   Basic theory, Journal of Geophysical Research: Space Physics, 108 (A9).

1109   Dimant, Y., and M. Oppenheim (2011), Magnetosphere-ionosphere coupling through E region

1110   turbulence: 2. Anomalous conductivities and frictional heating, Journal of Geophysical

1111   Research: Space Physics, 116 (A09304), doi:10.1029/2011JA016649.

1112   De Keyser, J., M. Roth, and J. Lemaire (1998), The magnetospheric driver of subauroral ion drifts,

1113   Geophys. Res. Lett., 25(10), https://doi.org/10.1029/98GL01135.

1114   Fallen, C. T., and B. J. Watkins (2013), Diurnal and seasonal variation of electron heat flux

1115   measured with the Poker Flat Incoherent-Scatter Radar, J. Geophys. Res. Space Physics, 118,

1116   5327–5332, doi:10.1002/jgra.50485.

1117   Figueiredo, S., T. Karlsson, and G. T. Marklund (2004), Investigation of subauroral ion drifts and

1118   related field-aligned currents and ionospheric Pedersen conductivity distribution, Ann.

1119   Geophys., 22, 923–934, doi:10.5194/angeo-22-923-2004.

1120   Forsyth, C., Rae, I. J., Mann, I. R., and Pakhotin, I. P. (2017), Identifying intervals of temporally

1121   invariant field-aligned currents from Swarm: Assessing the validity of single-spacecraft

1122   methods, J. Geophys. Res. Space Physics, 122, 3411– 3419, doi:10.1002/2016JA023708.

1123   Foster, J. C., and P. J. Erickson (2000), Simultaneous observations of E-region coherent

1124   backscatter and electric field amplitude at F-region heights with the Millstone Hill UHF radar,

1125   Geophysical Research Letters, 27 (19), 3177-180.

1126   Foster, J. C., and W. J. Burke (2002), SAPS: A new categorization for sub-auroral electric fields,

1127   Eos. Trans. AGU, 83(36), 393, doi:10.1029/2002EO000289.

1128   Foster, J. C., M. J. Buonsanto, M. Mendillo, D. Nottingham, F. J. Rich, and W. Denig (1994),

1129   Coordinated stable auroral red arc observations: Relationship to plasma convection, J. Geophys.

1130   Res., 99(A6), 11,429–11,439, doi:10.1029/93JA03140.

1131   Gallardo-Lacourt, B., Nishimura, Y., Donovan, E., Gillies, D. M., Perry, G. W., Archer, W. E., et

1132   al. (2018a). A statistical analysis of STEVE. Journal of Geophysical Research: Space Physics,

1133   123, 9893–9905. https://doi.org/10.1029/2018JA025368

Gallardo-Lacourt, B., Liang, J., Nishimura, Y., and Donovan, E. (2018b). On the origin of STEVE: Particle precipitation or ionospheric skyglow? *Geophys. Res. Lett.*, 45,7968– 7973. https://doi.org/10.1029/2018GL078509

Gallardo-Lacourt, B., Nishimura, Y., Lyons, L. R., Mishin, E. V., Ruohoniemi, J. M., Donovan, E. F., Angelopoulos, V., & Nishitani, N. (2017). Influence of auroral streamers on rapid evolution of ionospheric SAPS flows. *Journal of Geophysical Research: Space Physics*, 122, 12,406– 12,420. https://doi.org/10.1002/2017JA024198

Galperin, Y. I., Y. N. Ponomarov, and A. G. Zosinova (1973), Direct measurements of ion drift velocity in the upper atmosphere during a magnetic storm, Kosm. Issled., 11, 273.

Gillies, D. M., E. Donovan, D. Hampton, J. Liang, M. Connors, Y. Nishimura, B. Gallardo-Lacourt, and E. Spanswick, First observations from the TREx Spectrograph: the Optical Spectrum of STEVE and the Picket Fence Phenomena, Geophysical Research Letters, 46. https://doi.org/10.1029/2019GL083272

Gillies, D. M., Liang, J., Donovan, E., & Spanswick, E. (2020). The apparent motion of STEVE and the Picket Fence phenomena. *Geophysical Research Letters*, 47, e2020GL088980. https://doi.org/10.1029/2020GL088980

Goodwin, L. V., J.-P. St.-Maurice, H. Akbari, R. J. Spiteri (2018), Incoherent Scatter Spectra Based On Monte Carlo Simulations of Ion Velocity Distributions Under Strong Ion Frictional Heating, Radio Science, 10.1002/2017RS006468, 53, 3, 269-287.

Grubbs, G., Michell, R., Samara, M., Hampton, D., Hecht, J., Solomon, S., & Jahn, J. M. (2018). A comparative study of spectral auroral intensity predictions from multiple electron transport

models. Journal of Geophysical Research: Space Physics, 123, 993–1005. https://doi.org/10.1002/2017JA025026.

Harding, B. J., Mende, S. B., Triplett, C. C., & Wu, Y.-J. J. (2020). A mechanism for the STEVE continuum emission. *Geophysical Research Letters*, 47, 2020GL087102. https://doi.org/10.1029/2020GL087102

He, F., X.-X. Zhang, and B. Chen (2014), Solar cycle, seasonal, and diurnal variations of subauroral ion drifts: Statistical results, J. Geophys. Res. Space Physics, 119, 5076–5086, doi:10.1002/2014JA019807.

Heelis, R. A., Bailey, G. J., Sellek, R., Moffett, R. J., and Jenkins, B. (1993), Field-aligned drifts in subauroral ion drift events, J. Geophys. Res., 98(A12), 21493-21499, doi:10.1029/93JA02209.

Huba, J. D., Joyce, G., & Fedder, J. A. (2000). SAMI2 (Sami2 is another model of the ionosphere): A new low‐latitude ionosphere model. Journal of Geophysical Research, 105, 23,035–23,054.

Hudson, M. K., and M. C. Kelley (1976), The temperature gradient instability at the equatorward edge of the ionospheric plasma trough, J. Geophys. Res., 81, 3913– 3918.

Hysell, D., R. Miceli, and J. Huba (2013), Implications of a heuristic model of auroral Farley Buneman waves and heating, Radio Science, 48 (5), 527-534.

Jenkins, B., G. J. Bailey, A. E. Ennis, and R. J. Moffett (1997), The effect of vibrationally excited nitrogen on the low-altitude ionosphere, Ann. Geophys., 15, 1422–1428.02. https://doi.org/10.1007/s00585-997-1422-2

1176   Keller, H. B. (1971), A new difference scheme for parabolic problems, Numerical solution of

1177   partial differential equations-II, ed. B. Hubbard, 327-350, Academic press.

1178   Kelley, M. C. (2009), The Earth's Ionosphere, Plasma Physics and Electrodynamics, Int. Geophys.

1179   Ser., 2nd ed., Elsevier, New York.

1180   Liang J., B. Yang, E. Donovan, J. Burchill, and D. Knudsen (2017), Ionospheric electron heating

1181   associated with pulsating auroras: A Swarm survey and model simulation, J. Geophys. Res.

1182   Space Physics, 122, 8781–8807, doi:10.1002/2017JA024127.

1183   Liang, J., E. Donovan, B. Jackel, E. Spanswick, and M. Gillies (2016), On the 630 nm red-line

1184   pulsating aurora: Red-line Emission Geospace Observatory observations and model

1185   simulations, J. Geophys. Res. Space Physics, 121, 7988–8012, doi:10.1002/2016JA022901.

1186   Liang, J., Donovan, E., Connors, M., Gillies, D., St-Maurice, J. P., Jackel, B., et al. (2019). Optical

1187   spectra and emission altitudes of double-layer STEVE: A case study. *Geophysical Research*

1188   *Letters*, 46, 13630– 13639. https://doi.org/10.1029/ 2019GL085639

1189   Liang, J., Zou, Y., Nishimura, Y., Donovan, E., Spanswick, E., & Conde, M. (2021). Neutral wind

1190   dynamics preceding the STEVE occurrence and their possible preconditioning role in STEVE

1191   formation. *Journal of Geophysical Research: Space Physics*, 126,

1192   e2020JA028505 https://doi.org/10.1029/2020JA028505

1193   Liu, J., W. Wang, M. Oppenheim, Y. Dimant, M. Wiltberger, and S. Merkin (2016), Anomalous

1194   electron heating effects on the E region ionosphere in TIEGCM, Geophys. Res. Lett., 43, 2351–

1195   2358, doi:10.1002/2016GL068010.

1196   Loranc, M., and St-Maurice, J.-P. (1994), A time-dependent gyro-kinetic model of thermal ion

1197   upflows in the high-latitude *F* region, *J. Geophys. Res.*, 99(A9), 17429– 17451,

1198   doi:10.1029/93JA01852.

1199   Lyons, L. R., Nishimura, Y., Gallardo-Lacourt, B., Nicolls, M. J., Chen, S., Hampton, D.

1200   L., … Angelopoulos, V. (2015). Azimuthal flow bursts in the inner plasma sheet and possible

1201   connection with SAPS and plasma sheet earthward flow bursts. *Journal of Geophysical*

1202   *Research: Space Physics*, **120**, 5009– 5021. https://doi.org/10.1002/2015JA021023

1203   MacDonald, E. A., Donovan, E., Nishimura, Y., Case, N., Gillies, D. M., Gallardo-Lacourt, B., et

1204   al. (2018). New science in plain sight: Citizen Scientists lead to the discovery of optical

1205   structure in the upper atmosphere. Science Advances, 4(3), eaaq0030. https://doi.org/10.1126/

1206   sciadv.aaq0030

1207   Maruyama, N. (2020). Storms and substorms—The new whole system approach and future

1208   challenges, 10.1016/B978-0-12-814782-5.00009-1.

1209   Mende, S. B., Harding, B. J., & Turner, C. (2019). Subauroral green STEVE arcs: Evidence for

1210   low-energy excitation. *Geophysical Research Letters*, 46, 14256–

1211   14262. https://doi.org/10.1029/2019GL086145

1212   Milikh, G., and Y. S. Dimant (2003), Model of anomalous electron heating in the E region: 2.

1213   Detailed numerical modeling, Journal of Geophysical Research: Space Physics, 108 (A9).

1214   Milikh, G. M., L. P. Goncharenko, Y. S. Dimant, J. P. Thayer, and M. A. McCready (2006),

1215   Anomalous electron heating and its effect on the electron density in the auroral electrojet,

1216   Geophys. Res. Lett., 33, L13809, doi:10.1029/2006GL026530.

1217 Mishin, E., Nishimura, Y., and Foster, J. (2017), SAPS/SAID revisited: A causal relation to the

1218 substorm current wedge, *J. Geophys. Res. Space Physics*, 122, 8516– 8535,

1219 doi:10.1002/2017JA024263.

1220 Moffett, R. J., A. E. Ennis, G. J. Bailey, R. A. Heelis, and L. H. Brace (1998), Electron

1221 temperatures during rapid subauroral ion drift events, Ann. Geophys., 16, 450 – 459

1222 Moffett, R. J., G. J. Bailey, and B. Jenkins (1992b), Effects of greatly increased O+ loss in the

1223 ionospheric F-region, Planet. Space Sci., 40, 1631

1224 Moffett, R. J., R. A. Heelis, R. Sellek, and G. J. Bailey (1992a), The temporal evolution of the

1225 ionospheric signatures of subauroral ion drifts. Planet. Space Sci., 40, 663.

1226 Newton, G. P., J. C. G. Walker, and P. H. E. Meijer (1974), Vibrationally excited nitrogen in stable

1227 auroral red arcs and its effect on ionospheric recombination, J. Geophys. Res., 79, 3807 – 3818.

1228 Nishimura, Y., Gallardo-Lacourt, B., Zou, Y., Mishin, E., Knudsen, D. J., Donovan, E. F., et al

1229 (2019). Magnetospheric signatures of STEVE: Implication for the magnetospheric energy

1230 source and inter-hemispheric conjugacy. Geophysical Research Letters, 46.

1231 https://doi.org/10.1029/2019GL082460.

1232 Nishimura, Y., Donovan, E. F., Angelopoulos, V., & Nishitani, N. (2020). Dynamics of auroral

1233 precipitation boundaries associated with STEVE and SAID. *Journal of Geophysical Research:*

1234 *Space Physics*, 125, e2020JA028067. https://doi.org/10.1029/2020JA028067.

1235 Noël, J., St.-Maurice, J., and Blelly, P. (2000), Nonlinear model of short-scale electrodynamics in

1236 the auroral ionosphere. *Annales Geophysicae* **18,** 1128–1144. https://doi.org/10.1007/ s00585-

1237 000-1128-1.

1238 Noël, J.-M. A., J.-P. S.-Maurice, and P.-L. Blelly (2005), The effect of E-region wave heating on

1239 electrodynamical structures, Ann. Geophys., 23, 2081– 2094, doi:10.5194/angeo-23-2081-

1240 2005.

1241 Pandya, S. H., & Joshipura, K. N. (2014). Ionization of metastable nitrogen and oxygen atoms by

1242 electron impact: Relevance to auroral emissions. Journal of Geophysical Research: Space

1243 Physics, 119, 2263–2268. https://doi.org/10.1002/2013JA019208

1244 Pavlov, A. (2014). Photochemistry of ions at D-region altitudes of the ionosphere: A review.

1245 Surveys in Geophysics, 35(2), 259–334.

1246 Pavlov A. V. (1998), New electron energy transfer rates for vibrational excitations of N2 , Ann.

1247 Geophys., 16, 176–182.

1248 Pavlov, A. V., and M. J. Buonsanto (1996), Using steady state vibrational temperatures to model

1249 effects of N2* on calculations of electron densities, J. Geophys. Res., 101, 26,941– 26,945.

1250 Press, W. H., S. A. Teukolsky, W. T. Vetterling, and B. P. Flannery (2007), Numerical Recipes

1251 3rd Edition: The Art of Scientific Computing (3rd. ed.). Cambridge University Press, USA.

1252 Puhl-Quinn, P. A., H. Matsui, E. Mishin, C. Mouikis, L. Kistler, Y. Khotyaintsev, P. M. E. Décréau,

1253 and E. Lucek (2007), Cluster and DMSP observations of SAID electric fields, J. Geophys. Res.,

1254 112, A05219, doi:10.1029/2006JA012065.

1255 Rees, M. H., and R. G. Roble (1975), Observations and theory of the formation of stable auroral

1256 red arcs, Rev. Geophys., 13(1), 201–242, doi:10.1029/RG013i001p00201.

1257 Richards, P. G. (2001), Seasonal and solar cycle variations of the ionospheric peak electron density:

1258 Comparison of measurement and models, J. Geophys. Res., 106(A7), 12803– 12819,

1259 doi:10.1029/2000JA000365.

Richmond, A. D., E. C. Ridley, and R. G. Roble (1992), A thermosphere/ionosphere general circulation model with coupled electrodynamics, *Geophys. Res. Lett.*, **19**, 601–604, doi:10.1029/92GL00401

Ridley,A. J., Y. Deng, and G. Tóth (2006), The global ionosphere–thermosphere model, Journal of Atmospheric and Solar-Terrestrial Physics, Volume 68, Issue 8, 839-864.

Robinson, T. (1986), Towards a self-consistent non-linear theory of radar auroral backscatter, Journal of atmospheric and terrestrial physics, 48 (5), 417-422.

Schunk, R. W., Banks, P. M., and Raitt, W. J. (1976), Effects of electric fields and other processes upon the nighttime high-latitude F layer, J. Geophys. Res., 81(19), 3271–3282, doi:10.1029/JA081i019p03271.

Schunk, R., and A. Nagy (2009), Ionospheres: physics, plasma physics, and chemistry, Cambridge university press.

Semeter, J., Hunnekuhl, M., MacDonald, E., Hirsch, M., Zeller, N., Chernenkoff, A., & Wang, J. (2020). The mysterious green streaks below STEVE. AGU Advances, 1, e2020AV000183. https://doi.org/10.1029/2020AV000183.

Schmeltekopf, A. L., E. E. Ferguson, and F. C. Fehsenfeld (1968), Afterglow studies of the reactions He^+, He (2^3S), and O^+ with vibrationally excited N_2, J. Chem. Phys., 48, 2966–2973.

Sinnhuber, M., Nieder, H., & Wieters, N. (2012). Energetic particle precipitation and the chemistry of the mesosphere/lower thermosphere. Surveys in Geophysics, 33(6), 1281–1334.

Solomon, S. C., P. B. Hays, and V. J. Abreu (1988), The auroral 6300 Å emission: Observations and modeling, J. Geophys. Res., 93, 9867– 9882, doi:10.1029/JA093iA09p09867.

Solomon, S. C. (2017), Global modeling of thermospheric airglow in the far-ultraviolet, J. Geophys. Res., 122, doi:10.1002/2017/JA024314.

Spiro, R., R. Heelis, and W. Hanson (1979), Rapid subauroral ion drifts observed by Atmospheric Explorer C, *Geophys. Res. Lett.*, **6**, 657–660.

Strickland, D. J., J. Bishop, J. S. Evans, T. Majeed, P. M. Shen, R. J. Cox, R. Link, and R. E. Huffman (1999), Atmospheric Ultraviolet Radiance Integrated Code (AURIC): Theory, software architecture, inputs, and selected results, J. Quant. Spectrosc. Radiat. Transfer, 62, 689– 742.

St-Maurice, J.-P., and Laneville, P. J. (1998), Reaction rate of O^+ with O_2, N_2, and NO under highly disturbed auroral conditions, *J. Geophys. Res.*, 103(A8), 17519– 17521, doi:10.1029/98JA01387.

St-Maurice, J.-P., & Goodwin, L. (2021). Revisiting the behavior of the *E*-region electron temperature during strong electric field events at high latitudes. *Journal of Geophysical Research: Space Physics*, 126, e2020JA028288. https://doi.org/10.1029/2020JA028288

St-Maurice, J.-P., C. Cussenot, and W. Kofman (1999), On the usefulness of E region electron temperatures and lower F region ion temperatures for the extraction of thermospheric parameters: a case study, Annales Geophysicae, 17 (9), 1182-1198.

Sydorenko, D., and Rankin, R. (2013), Simulation of O^+ upflows created by electron precipitation and Alfvén waves in the ionosphere, *J. Geophys. Res. Space Physics*, 118, 5562– 5578, doi:10.1002/jgra.50531.

Thomas, G. E. (1963), Lyman α scattering in the Earth's hydrogen geocorona: 1., J. Geophys. Res., 68(9), 2639– 2660, doi:10.1029/JZ068i009p02639.

Wang, W., Talaat, E. R., Burns, A. G., Emery, B., Hsieh, S., Lei, J., and Xu, J. (2012), Thermosphere and ionosphere response to subauroral polarization streams (SAPS): Model simulations, *J. Geophys. Res.*, 117, A07301, doi:10.1029/2012JA017656.

Williams, P., B. Jones, and G. Jones (1992), The measured relationship between electric field strength and electron temperature in the auroral E-region, Journal of atmospheric and terrestrial physics, 54 (6), 741-748.

Yadav, S., Shiokawa, K., Otsuka, Y., Connors, M., & St Maurice, J.-P. (2021). Multi-wavelength imaging observations of STEVE at Athabasca, Canada. Journal of Geophysical Research: Space Physics, 126, e2020JA028622. https://doi.org/10.1029/2020JA028622.

Yeh, H.-C., J. C. Foster, F. J. Rich, and W. Swider (1991), Storm time electric field penetration observed at mid-latitude, J. Geophys. Res., 96(A4),5707–5721, doi:10.1029/90JA02751.

Zettergren, M., and Semeter, J. (2012), Ionospheric plasma transport and loss in auroral downward current regions, J. Geophys. Res., 117, A06306, doi:10.1029/2012JA017637.

Zhu, J., A. J. Ridley, and Y. Deng (2016), Simulating electron and ion temperature in a global ionosphere thermosphere model: Validation and modeling an idealized substorm, J. Atmos. So. Terr. Phys., 138, 243-260.

1319 Zou, S., L. R. Lyons, and Y. Nishimura (2012), Mutual evolution of aurora and ionospheric

1320   electrodynamic features near the Harang reversal during substorms, *Geophysical Monograph*

1321   *Series*, *197*, 159–169, doi:10.1029/2011GM001163.

1322

Figure Caption:

1324 Figure 1. The slope of Te enhancement versus V_E for the AEH calculation used in this study.

1325

1326 Figure 2. (a) POES/NOAA-17 observations. The upper panel gives the Total Electron detector (TED)
1327 observations of the total electron precipitation fluxes; the bottom panel shows the energy channel where
1328 the differential electron fluxes maximize in the 0^0-sensor and 30^0-sensor (both sensors are within the loss
1329 cone). (b) Copied from Gillies et al. [2019] showing the optical spectra of STEVE compared to its ambient
1330 neighbors. (c) The 427.8 blue-line emission intensity derived from TREx spectrograph measurement as a
1331 function of MLAT. In (a) and (c), a vertical dashed line marks the position of STEVE arc.

1332

1333 Figure 3. Simulation outcome of altitude-MLAT profile of Te at six elapsed times. The latitudinal profiles
1334 of SAID and the background precipitation are plotted on top for reference. Zero relative latitude indicates
1335 the center of SAID.

1336

1337 Figure 4. Same as Figure 3 but for Ti.

1338

1339 Figure 5. Same as Figure 3 but for Ne.

1340

1341 Figure 6. Comparison between the simulation runs with ion Pedersen drift (left-side) and without ion
1342 Pedersen drift (right-side). In each side, from top to bottom panels are the latitude-altitude profile of Te and
1343 Ne, and the latitudinal profile of Pedersen conductance, at t=10 min.

1344

1345 Figure 7. Altitudinal profile of densities of Ne, NO+ and O+ at the center of SAID at (a) *t*=0; (b) t=1 min;
1346 (c) t=5 min; and (d) t=10 min. In subfigures (b)-(d), The initial (*t*=0) Ne profile is plotted in dotted line for
1347 reference.

1348

1349 Figure 8. Altitudinal profile of Pedersen conductivity at the center of SAID at (a) t=30 sec; (b) t=-2 min;

1350 (c) t=5 min; and (d) t=10 min. The initial (t=0) Pederson conductivity profile is plotted in dotted line for

1351 reference.

1352

1353 Figure 9. latitudinal profiles of Σ_P and FAC at different elapsed times. The latitudinal profiles of SAID and

1354 the background precipitation are plotted on top for reference.

1355

1356 Figure 10. Latitude-altitude profile of Ne, and the latitudinal profile of FAC at t=15 min for a new run with

1357 higher flow poleward of SAID. The latitudinal profiles of SAID and the background precipitation are

1358 plotted on top for reference.

1359

1360 Figure 11. Comparison between the simulation runs with extra heat flux (left-side, first run in the paper)

1361 and without extra heat flux (right-side, new run). In each side, form top to bottom panels are the latitude-

1362 altitude profile of Te and Ne, and the latitudinal profile of FAC, at t=15 min.

1363

1364 Figure 12. Latitudinal profiles of plasma flows, Te, Ti, and Ne, averaged over 100-150 km altitudes.

1365